Measurement report: Observational Analysis of Mode-Dependent Fog Droplet Size Distribution Evolution and Improved Parameterization Using Segmented Gamma and Lognormal Fitting

Jingwen Zhang[1,2,3], Xiaoli Liu[1,2,3], Zhenya An[4], Jingjing Lv[1,2], Dan Xu[1,2]

[1]State Key Laboratory of Climate System Prediction and Risk Management, Nanjing University of Information Science and Technology, Nanjing, 210044, China
[2]China Meteorological Administration Aerosol-Cloud and Precipitation Key Laboratory, Nanjing University of Information Science and Technology, Nanjing, 210044, China
[3]School of Atmospheric Physics, Nanjing University of Information Science and Technology, Nanjing, 210044, China
[4]College of Meteorology and Oceanology, National University of Defense Technology, Changsha, 410000, China

Correspondence to: Xiaoli Liu (liuxiaoli2004y@nuist.edu.cn)

Abstract. ~~Influenced by numerous physical factors, the evolution of fog droplet size distributions (DSDs) during the fog lifecycle is not yet fully understood and difficult to represent realistically in numerical models, constraining the accuracy of fog forecasting.~~ Fog droplet size distributions (DSDs) evolve under the influence of many physical processes, yet their development through the fog lifecycle remains insufficiently understood and challenging to represent in numerical models, constraining the accuracy of fog forecasting. To improve understanding of the fog evolution, field observations under a polluted background were conducted during the winters of 2006-2009 and 2017-2018 in Nanjing, China. ~~Among the 27 observed fog events, microphysical properties such as fog number concentration (N_f), liquid water content (LWC), volume-mean radius (R_v) and effective radius (R_{eff}) vary substantially. The unimodal (3 μm), bimodal (3, 21 μm) and trimodal (around 3, 13, 21 μm) DSD were observed. As the fog developed, the DSDs evolved from unimodal to multimodal. The third mode centered at 13 μm in trimodal cases appeared after the other two modes, typically around the time LWC reached its maximum, corresponding to the mature stage of fog. For all mode types, the probability density function decreased with increasing N_f and LWC. R_v is generally greater than 4 μm and R_{eff} greater than 6 μm for trimodal DSDs. Based on the observational findings, a segmented gamma fitting was applied to the mean DSD with partition points at 10 and 21 μm. Comparison between microphysical parameters derived from the fitted DSD and those from observations indicates that the three-segment fitting provides more accurate estimates of N_f and LWC. Moreover, the three-segment gamma fitting substantially improves the representation of R_{eff}, absorption coefficient and optical thickness, with most deviations constrained within 20%.~~ Among the 27 observed fog events, microphysical properties including fog droplet number concentration (N_f), liquid water content (LWC), volume-mean radius (R_v), and effective radius (R_{eff}) varied substantially. Unimodal, bimodal, and trimodal DSDs were observed, with peak diameters of 3 μm for unimodal; 3 and 7-13 μm for bimodal; and 3, 9-15, and 21-25 μm for trimodal DSDs. The number of peaks and the peak diameters changed as fog developed. Trimodal DSD gradually shifted to bimodal

with peak diameters at 3 and 12-19 μm, usually around the time when LWC reached its maximum, corresponding to the mature stage of fog. The probability density function distributions of R_v and R_{eff} for bimodal DSDs were more concentrated than those for trimodal DSDs. Based on these observational features, segmented gamma and lognormal fits were applied to mean DSDs using partition points at 10 and 22 μm. Comparisons between microphysical parameters derived from the fitted DSD and observations show that three-segment fitting improved estimates of N_f and LWC and substantially enhanced the representation of R_{eff}, absorption coefficient, and optical thickness, with most deviations constrained within 20%.

设置了格式: 字体: (中文) +中文正文 (等线), (中文) 简体中文(中国大陆), (其他) 英语(英国)

1 Introduction

Composed of suspended small water droplets or individual ice crystals in the air near the surface, fog has multiple impacts ranging from transportation, vegetation, air quality, human health and economy (Gultepe et al., 2014; Jia et al., 2019; Lakra and Avishek, 2022). Due the sharp decline in visibility, long duration, wide spatial coverage associated with fog, it is essential and urgent to improve fog modeling and forecasting. ~~The formation and evolution of fog is driven by macro and microphysical processes including radiation, turbulent, aerosol activation and condensation (Mazoyer et al., 2022; Shao et al., 2023; Wang et al., 2020).~~ The formation and evolution of fog is driven by macro and microphysical processes including precipitation, radiation, advection, cloud-base lowering, turbulent, aerosol activation and condensation (Gultepe et al., 2007; Mazoyer et al., 2022; Shao et al., 2023; Wang et al., 2020). With different physical processes interact with each other nonlinearly, fog remains as a challenging problem for numerical weather prediction (NWP), even though progress have been made in recent years (Boutle et al., 2018; Martinet et al., 2020; Tudor, 2010).

In order to gain a better understanding in mechanisms of fog evolution, in situ observations have been conducted worldwide with different regions and aerosol backgrounds ~~(Elias et al., 2009; Gultepe et al., 2007, 2009; Haeffelin et al., 2010; Mazoyer et al., 2022)~~ (Elias et al., 2009; Gultepe et al., 2007, 2009; Gultepe and Milbrandt, 2007; Haeffelin et al., 2010; Mazoyer et al., 2022). Marked variabilities of microphysical parameters such as fog number concentration (N_f) and liquid water content (LWC) have been found. Fogs in polluted area show higher N_f due to higher aerosol number concentration (N_a), while in relative clean regions including mountains, rainforests and rural areas there are more big droplets, which contribute to LWC significantly (Gultepe and Milbrandt, 2010; Guo et al., 2015; Li et al., 2017; Nelli et al., 2024). Also, the fierce competition for water vapor associated with higher N_a suppresses the condensation growth in urban areas, resulting a lower N_f of large droplets and smaller dispersion (ε) in urban fog compared to clean regions (Ge et al., 2024).

Meteorological variables and large-scale processes strongly influence fog formation. In general, fog can be classified into two categories: airmass fog and frontal fog, which can be further divided into cold- and warm-advection fog, radiation fog, and sea fog etc. (WILLETT, 1928). Another fog-forming mechanism is the overall lowering of a cloud layer, including its cloud top (Koračin et al., 2014). Radiation fog typically forms near the surface under clear skies and weak winds associated with anticyclonic conditions. Its primary mechanism is radiative cooling, while opposing effects include upward soil heat flux and

the warming and moisture loss caused by turbulent mixing within the stable boundary layer (Brown, 1980; Roach, 1976; Turton and Brown, 1987). The advection fog is associated with the advection of a moist air mass with a temperature contrast relative to the underlying surface, which is mainly coastal but also can be observed over land (Friedlein, 2004). Advection-radiation fog is produced by the radiative cooling of moist air that has been advected inland from the ocean or another large water body (Ryznar, 1977). The C-FOG field campaign along the Atlantic Canada and northeastern U.S. coastlines showed that coastal fog was influenced by multiple weather systems, including northeastern high pressure, west-northwest low pressure, and tropical cyclonic activity (Gultepe et al., 2021). Another study in the region found that fog associated with cyclonic systems was consistently produced by cloud-base lowering and subsequent downward extension to the surface, whereas anticyclonic fog developed either from surface radiative cooling or from the downward extension of low-level stratus to the surface (Dorman et al., 2021).

The fog droplet size distribution is a key characteristic of fog microphysical processes (Niu et al., 2012), which is influenced by aerosol chemical composition and number concentration as well as various environment factors such as temperature, humidity, wind speed and direction (Mazoyer et al., 2017; Price, 2019). ~~The peak of the droplet number concentration spectrum in urban fog occurs at 3 μm, compared 3.5 μm in rural areas and 4.5 μm in rainforest regions. This suggests that aerosol particles serving as cloud condensation nuclei (CCN) in rural and rainforest areas are generally larger in size compared to those in urban environments (Ge et al., 2024).~~ Fog droplet size distributions (DSDs) often exhibit one or more distinct peaks, referred to as unimodal, bimodal, or trimodal DSD, and can be attributed to different origins of the fog and processes within it (Elias et al., 2015; Hammer et al., 2014; Sampurno Bruijnzeel et al., 2005). KUNKEL (1982) finds various shapes in DSDs measured in advection fogs. Many other studies have shown the existence of bimodal DSDs in mature radiation fogs (Meyer et al., 1980; Pinnick et al., 1978; Roach et al., 1976; Wendisch et al., 1998). Gultepe and Milbrandt (2007) reported DSD modes near 4 and 23 μm during winter fog events in the Toronto region. Boudala et al. (2022) investigated the seasonal and microphysical characteristics of fog at Cold Lake Airport in northern Alberta, Canada, and found that radiation fog exhibited a bimodal droplet spectrum with peaks at 4 μm and 17-25 μm. Mazoyer et al. (2022) observed that fog droplet size distribution (DSD) in a semi-urban area of Paris exhibited both single mode (about 11 μm) and double mode (about 11 and 22 μm). When the fog DSD is bimodal, there is a mass transfer from smaller droplets to larger droplets which may due to collision-coalescence process, while sedimentation by gravity speeds up the removal of fog droplets (Mazoyer et al., 2022). The initial fog DSD is influenced by environmental supersaturation and background aerosol properties. As visibility decreases and fog develops, the DSD broadens, transitioning from unimodal to multimodal. (Mazoyer et al., 2022). ~~In situ measurements conducted in Jinan, China revealed that when visibility is greater than 500 m, fog DSD is unimodal, with a peak at 4 μm. DSD broadened and became bimodal (5 and 14 μm) as visibility drops below 500 m. Trimodal DSDs (5, 14 and 22 μm) occurred when visibility was lower than 200 m (Wang et al., 2021a).~~ The characteristics of the DSD also strongly influence the optical properties of fog. Stewart and Essenwanger (1982) showed that the attenuation of electromagnetic radiation by fog depends sensitively on the shape of the droplet size distribution. The DSD and water vapor determine the overall optical properties of fog and its effects on visibility and radiative transfer together.

设置了格式: 字体: (中文) +中文正文 (等线), (中文) 简体中文(中国大陆), (其他) 英语(美国)

Integrated with in situ measurement, numerical experiment is a commonly used approach to gain a better understanding of the physical mechanism in fog. Over the past decade, numerous numerical experiments have been conducted to evaluate the fog forecasting capabilities and limitations of various mesoscale NWP models, leading to notable progress (Cui et al., 2019; Payra and Mohan, 2014). Despite WRF has made progress~~showed a well performance~~ in forecasting certain variables such as temperature and wind, it often struggles to capture the accurate fog lifecycle (Peterka et al., 2024; Román-Cascón et al., 2016). The simulated evolution of fog exhibits a sensitivity to the shape of the DSD comparable to its sensitivity to aerosol loading or cloud droplet number concentration (CDNC), yet it remains one of the least investigated and rarely adjusted components of microphysical parameterization schemes (Boutle et al., 2022).~~Fog development and characteristic are sensitive to the shape of the DSD in models (Boutle et al., 2022).~~ A simulation of a heavy fog event in North China Plain found that effective radius of fog droplet decreases~~increases~~ nonlinearly with aerosol number concentration (Jia et al., 2019). Since~~However, since~~ the effective radius was obtained under the assumption of a monodisperse DSD and the dispersion effect was neglected, it may have been overestimated or underestimated due to fog-aerosol interactions (Chen et al., 2016; Liu and Daum, 2002). Currently, fog DSDs are described using various spectral distribution functions such as exponential, gamma or lognormal functions in bulk and bin microphysical scheme (Kessler, 1969; Khain et al., 2015). However, the fog DSD exhibits strong spatial and temporal variability and evolves throughout the fog lifecycle, often displaying distinct features and deviating from idealized distributions due to turbulent mixing, radiative effects, and gravitational settling (Gultepe et al., 2007; Nelli et al., 2024; Tampieri and Tomasi, 1976; Wang et al., 2021).~~often displaying distinct features such as bimodality (Nelli et al., 2024; Wang et al., 2021b).~~ Such variabilities in DSD could cause substantial deviations from the predefined spectral distribution functions, further bringing challenges for fog parameterization (Khain et al., 2015; Lakra and Avishek, 2022). Therefore, a more physically consistent and adaptable representation of DSD is required to improve simulation reliability of fog evolvement.

In this study, based on the observation data of the 27 fog events obtained in Nanjing, China during the winters of 2006-2009, 2017-2018, we focus on the characteristics and evolution of DSDs, how they are associated with microphysical characteristics and how to improve the representation of multimodal size distributions using the gamma and lognormal function. The rest of the article is organized as follows. Section 2 describes the observation site and data. Section 3 presents the results of this study, including an overview of microphysics across 27 fog events, an analysis the fog lifecycle under different modes, the correlations between microphysical characteristics and varying DSD modes, and a refinement of the gamma and lognormal fitting approach with an evaluation of its performance. The main conclusions are presented in Sections 4.~~The discussion and main conclusions are presented in Sections 4 and 5.~~

2 Data Set and Methods

The field campaign was conducted during the winters of 2006-2009 and 2017-2018, with each campaign lasting approximately one month per year. The sampling site was located in the northwestern suburban area of Nanjing, Jiangsu Province, China (32.2° N, 118.7° E; 22 m above sea level.), north of the Yangtze River and surrounded by industrial facilities, residential areas,

and major roads (Niu et al., 2010, 2012). ~~The sampling site was located at Pancheng (32.2 °N, 118.7 °E; 22 m above sea level), Jiangsu Province, China, north of the Yangtze River and was surrounded by industrial facilities, residential areas, and busy roads (Niu et al., 2010, 2012).~~ The DSD was measured with a fog monitor (FM-100) from Droplet Measurement Technologies (DMT, USA) with diameters ranging from 1~~0~~ to 50 μm into 20 bins, at a sampling frequency of 1 Hz. The width of each bin is 2 μm for the first 10 bins and 3 μm for the last 10 bins. To exclude the influence of large unactivated aerosol particles, data from the first bin (1~~0~~-2 μm) are omitted (Lu et al., 2013). Fog with N_f > 10 cm^{-3} and LWC > 10^{-3} g m^{-3} was identified (Lu et al., 2020; Wang et al., 2021~~b~~). Microphysical characteristics including fog number concentration (N_f), liquid water content (LWC), volume-mean radius (R_v), effective radius (R_{eff}), dispersion (ε), autoconversion threshold (T) and first bin strength (FBS) were calculated through following formulas:

$$N_f = \sum n(r) \quad (1)$$

$$LWC = 1 \times 10^{-6} \rho \sum \frac{4\pi}{3} r^3 n(r) \quad (2)$$

$$R_v = \left(\frac{\sum n(r) r^3}{N_f}\right)^{\frac{1}{3}} \quad (3)$$

$$R_{eff} = \frac{\sum n(r) r^3}{\sum n(r) r^2} \quad (4)$$

$$\sigma = \left(\frac{n(r)(r-\bar{r})^2}{N_f}\right)^{\frac{1}{2}} \quad (5)$$

$$\varepsilon = \frac{\sigma}{\bar{r}} \quad (6)$$

$$T = \frac{P}{P_0} = \left[\frac{\int_{r_c}^{\infty} r^6 n(r) dr}{\int_0^{\infty} r^6 n(r) dr}\right]\left[\frac{\int_{r_c}^{\infty} r^3 n(r) dr}{\int_0^{\infty} r^3 n(r) dr}\right] \quad (7)$$

$$FBS = \frac{N_{1st}}{N_f} \quad (8)$$

where ρ is the density of water, r is the fog droplet diameter of each bin, $\bar{r}$ is the mean arithmetic radius defined with $\bar{r} = \sum \frac{n(r) r}{N_f}$, r_c is defined with $r_c \approx 4.09 \times 10^{-4} \beta_{con}^{\frac{1}{6}} \frac{N^{\frac{1}{6}}}{LWC^{\frac{1}{3}}}$, in which $\beta_{con} = 1.15 \times 10^{23}$, N_{1st} is the number concentration of the first bin (2-4 μm) following the exclusion of the 1~~0~~-2 μm bin.

Because visibility observations were unavailable for fog cases 1-3 and 18-20, visibility for these cases was estimated using the observed fog droplet spectra and the microphysical parameterization scheme developed by Gultepe (2006), based on the extinction theory of visible light in fog:

$$V = \frac{-\ln \alpha}{\beta_{ext}} \quad (9)$$

in which $\beta_{ext} = \pi \sum Q_{ext} n(r) r^2 dr$ (10)

where α is the constant threshold, typically set to 0.02, β_{ext} represents the extinction coefficient, Q_{ext} is the Mie extinction efficiency, which depends on particle radius, number concentration, and the wavelength of visible light. When droplet size exceeds about 4 μm, Q_{ext} approaches a constant value of 2. For smaller droplets (less than 4μm), Q_{ext} varies between 0.9 and 3.8 (Brenguier et al., 2000; KOENIG, 1971).

To determine the number of peak modes and mode positions, each fog DSD was sequentially fitted with unimodal (i=1), bimodal (i=2), and trimodal (i=3) gamma and lognormal distributions as show below:

For the gamma distribution:

$$n(D) = \sum_{i=1}^{3} n_i(D) = \sum_{i=1}^{3} N_{0,i} D^{\mu_i} e^{-\lambda_i D} \quad (11)$$

where D is the droplet diameter, $n(D)$ is the number concentration for each bin, N_0, μ and λ are three distribution parameters of gamma. For the lognormal distribution:

$$n(D) = \sum_{i=1}^{3} n_i(D) = \sum_{i=1}^{3} \frac{n_i}{2\pi^{1/2} D_i ln\sigma_{g,i}} \exp\left(-\frac{(lnD_i - lnD_{g,i})^2}{2(ln\sigma_{g,i})^2}\right) \quad (12)$$

where D is the droplet diameter, $n(D)$ is the number concentration for each bin, D_g is the geometric mean diameter and σ_g is the geometric standard deviation. By setting the derivative to zero and solving, the peak diameter (D_{peak}) can be expressed as a function of the fitting parameter D_g and σ_g:

$$D_{peak} = D_g \exp\left(-(ln\sigma_g)^2\right) \quad (13)$$

Details on the starting points and upper and lower bounds used for fitting Eq. (11) and Eq. (12) for each value of i are provided in the appendix (Figure A1).

For each DSD, unimodal, bimodal, and trimodal fits using both the gamma and lognormal distribution were evaluated. The Akaike Information Criterion (AIC) and the Bayesian Information Criterion (BIC) were used to determine which of the three fits provides the best representation of the given DSD within each distribution type, and this fit was considered as the optimal fit. AIC and BIC are two influential and widely used model selection criteria in machine learning, engineering, and related scientific fields (Akaike, 1974; Schwarz, 1978; Zhang et al., 2023). AIC provides a numerical basis for ranking competing models by their information loss in approximating the unknown true process, with the model yielding the lowest AIC considered the best approximating model (Symonds and Moussalli, 2011). BIC is consistent in the sense that it selects the true model with probability approaching one. A lower BIC corresponds to a higher posterior probability for the model and is therefore regarded as indicating a better model (Chakrabarti and Ghosh, 2011). The corresponding formulas are as follows:

$$AIC = -2\ln(\hat{L}) + 2p \quad (14)$$

$$BIC = -2\ln(\hat{L}) + p\ln(N) \quad (15)$$

where $\hat{L}$ is the maximum likelihood estimate, p is the number of independently adjusted parameters, N is the number of samples.

Within each distribution type, the unimodal, bimodal, and trimodal fits are compared, and the one with the lowest AIC and BIC was considered the optimal fit of the given DSD. Accordingly, both the gamma and lognormal functions yield their own

sets of optimal fits, each providing the number of peaks and the corresponding peak diameters for every DSD. As shown in Figure 1a, the multimodal composite distributions yield significantly lower AIC and BIC values compared to the original single mode distribution (i = 1), indicating a more accurate representation of the DSD. Additionally, N_f, LWC, R_v, and R_{eff} retrieved from the optimal fit show much smaller deviations from observations than those from traditional single mode fits, further confirming the effectiveness of this approach. A comparison between the optimal fit results using gamma and lognormal distributions reveals that the lognormal distribution yield smaller absolute deviations of N_f, LWC, R_v, and R_{eff} (Figure 1b), therefore in this study, the lognormal fitting results are used to determine the number of peak modes and their corresponding peak diameters.

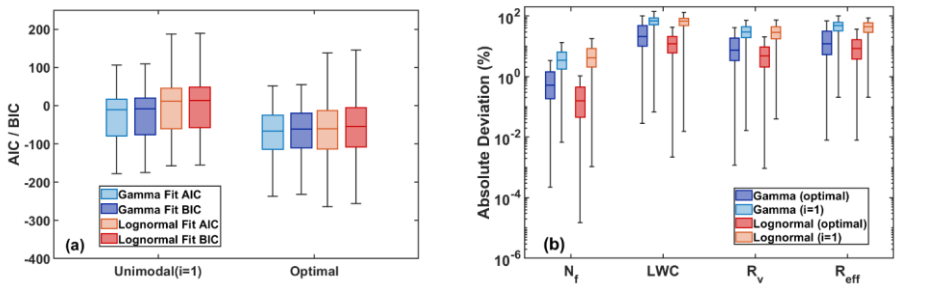

Figure 1 Distributions of AIC/BIC values for optimal gamma and lognormal fits and the original distribution forms (a), and their absolute deviations between the retrieved and observed microphysical properties (b).

Given that temporal resolution may influence the identification of DSD peak mode numbers and peak diameters, we derived these quantities using both 1-min and 5-min averaged DSDs, classified the fog cases, and analyzed the distributions of peak diameters. The two resolutions produced only minor differences in case type and modal-diameter distributions (Figure 2). Detailed classifications and modal-diameter tables for both temporal resolutions are provided in the appendix (Table A2). To reduce the influence of noise, a 5-min averaging interval was used in this work.

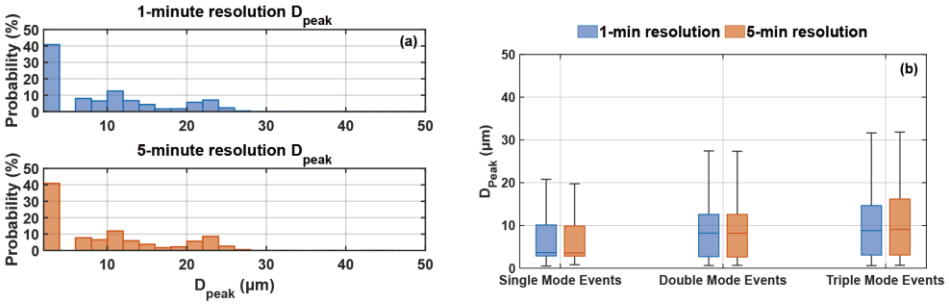

Figure 2 (a) The D_{peak} distributions of all DSDs at 1-min and 5-min resolution, and (b) the D_{peak} distributions by fog type at both resolutions

设置了格式: 字体: (中文) +中文正文 (等线), (中文) 简体中文(中国大陆)

3 Results

3.1 Overview of fog microphysics

The fog type, meteorological variables (temperature, wind speed), visibility, and summary statistics of N_f, LWC, R_v, R_{eff}, ε, T and FBS for each event are provided in Table A1 of Appendix. Among the 27 fog events, 14 were classified as radiation fog, 8 as radiation-advection fog, 4 as advection fog and 1 was caused by the rain. Compared to other fog types, radiation-advection fog typically exhibits longer duration, slightly higher wind speed and temperature, and is more frequently associated with trimodal DSDs.~~Summary statistics of N_f, LWC, R_v, R_{eff}, ε, T and FBS for each event are provided in Table A1 of Appendix.~~ The average N_f, LWC, R_v and R_{eff} vary over the ranges of 25-586 cm^{-3}, 0-0.27 g m^{-3}, 1.6-6 μm, 1.9-8.2 μm~~25-587 cm^{-3}, 0-0.28 g m^{-3}, 1.6-6 μm, 1.9-8.3 μm~~, respectively, which shows greater N_f, lower LWC and smaller droplet sizes comparing to semi-urban area in Paris, France (Mazoyer et al., 2022) and rainforest area in Xishuangbanna, China (Wang et al., 2021~~b~~). In the meantime, significant variability in the microphysical properties is observed between different events. Both unimodal and multimodal DSDs are observed and in some cases, a transition from unimodal to multimodal occurs as fog develops. Unimodal (peak at 3 μm), bimodal (peak at 3, 7-13 μm) and trimodal (peak at 3, 9-15, 21-25 μm) DSD account for 22%, 33%, and 44% of the 27 cases, respectively. Trimodal cases show a mean LWC twice that of unimodal cases, while bimodal cases have higher average N_f. Trimodal cases also feature significantly higher autoconversion thresholds (T), larger droplet sizes, and lower FBS. A high dispersion value of 0.72 further indicates a broader DSD in these events.

~~The number of modes for each event was determined based on the presence of local minima in the DSD (Mazoyer et al., 2022). Among the 27 fog events, both unimodal and multimodal DSDs are observed. In some cases, a transition from unimodal to multimodal occurs as fog develops. Unimodal (3 μm), bimodal (3, 21 μm) and trimodal (around 3, 13, 21 μm) DSD account~~

~~for 15%, 52%, and 33% of the 27 cases, respectively. Trimodal cases show greater N_f, LWC with bigger droplets and lower FBS. The average R_v and R_{eff} in trimodal cases are approximately twice those in unimodal cases, accompanied by a significantly higher autoconversion threshold (T). A high dispersion of 0.82 also indicates a broader DSD in trimodal events.~~

Table 1 Microphysical characteristics of single mode, double mode and triple mode fog events, the first row shows the mean values, in the parentheses are the 25th and 75th percentiles of each characteristic

~~Type~~	~~Peak Diameter (μm)~~	~~N_f(cm^{-3})~~	~~LWC(g m^{-3})~~	~~R_v(μm)~~	~~R_{eff}(μm)~~	~~T~~	~~ε~~	~~FBS(%)~~
~~Single-mode~~	~~3~~	~~168.95 (45.14, 240.22)~~	~~0.03 (0.003, 0.03)~~	~~2.91 (2.23, 3.44)~~	~~4.46 (2.99, 5.31)~~	~~0.02 (0, 0.01)~~	~~0.56 (0.43, 0.67)~~	~~67.49 (56.99, 78.54)~~
~~Double-mode~~	~~3, 21~~	~~235.52 (84.25, 327.64)~~	~~0.11 (0.01, 0.15)~~	~~4.05 (3.17, 4.84)~~	~~6.55 (5.07, 7.93)~~	~~0.12 (0.01, 0.15)~~	~~0.72 (0.63, 0.81)~~	~~56.56 (44.92, 67.91)~~
~~Triple-mode~~	~~3, 11/13/15, 21~~	~~290.70 (192.03, 383.86)~~	~~0.23 (0.11, 0.34)~~	~~5.53 (4.90, 6.21)~~	~~8.43 (7.43, 9.47)~~	~~0.25 (0.05, 0.43)~~	~~0.82 (0.78, 0.86)~~	~~44.05 (36.41, 51.47)~~
Type	Peak Diameter (μm)	N_f(cm^{-3})	LWC(g m^{-3})	R_v(μm)	R_{eff}(μm)	T	ε	FBS(%)
Single-mode	3	199.61 (43.22, 203.40)	0.06 (0.004, 0.03)	3.30 (2.50, 4.18)	5.47 (3.73, 7.02)	0.04 (0, 0.06)	0.63 (0.49, 0.78)	68.28 (56.21, 74.74)
Double-mode	3, 7-13	242.36 (76.78, 373.95)	0.08 (0.006, 0.12)	3.59 (2.72, 4.52)	5.38 (3.79, 6.80)	0.03 (0, 0.02)	0.66 (0.53, 0.78)	59.05 (47.61, 67.13)
Triple-mode	3, 9-15, 21-25	230.42 (85.38, 327.41)	0.12 (0.01, 0.18)	4.22 (3.12, 5.37)	6.73 (4.80, 8.50)	0.16 (0.01, 0.26)	0.72 (0.62, 0.83)	55.24 (40.29, 68.46)

格式化表格

Figure 3~~1~~ shows the mean DSDs for fog events with different modes, as well as the overall mean DSD across all cases. For droplet sizes smaller than 20 μm, the spectral distributions across cases with different modes are similar, particularly for droplets below 6 μm. And the mean spectrum closely matching that of the trimodal cases.~~The overall mean spectrum lies between the mean DSDs of bimodal and trimodal events as expected. The distributions exhibit similar N_f at the small-droplet end (around 3 μm). However, as droplet size increases, the unimodal spectrum shows a sharp decrease.~~ As aerosol activation is governed by environmental supersaturation and the aerosols hygroscopic properties (Shen et al., 2018; Wang et al., 2019), the similar N_f at the small-droplet end may suggest that aerosols continue to activate throughout fog development in both unimodal and multimodal cases. For diameters above 20 μm, the mean N_f in single-mode and double-mode cases decrease rapidly. Above approximately 35 μm, double-mode cases exhibit the lowest mean N_f. Triple-mode events consistently exhibit the broadest DSD and highest N_f of large droplets, consistent with their higher LWC and greater dispersion noted earlier.

In the following section, five representative cases are selected to examine the lifecycle characteristics of fog events with different modes and the evolution of DSDs throughout the stages of fog formation, development, and dissipation.

~~Note that the mean DSD of trimodal events shows higher N_f than that of bimodal cases in the 10-35 μm range, but lower N_f beyond 35 μm. This raises three questions: What are the differences in lifecycle characteristics among fog events with varying numbers of modes? How does the DSD evolve throughout the stages of fog formation, development, and dissipation? What is the relationship between the number of modes and microphysical parameters?~~

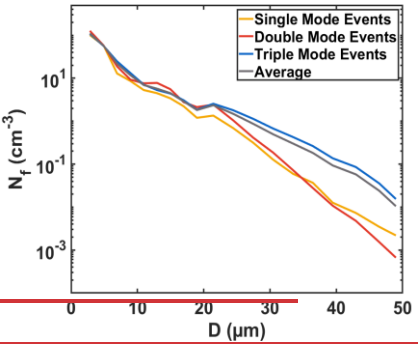

Figure 3 Average spectrums of fog events with different modes

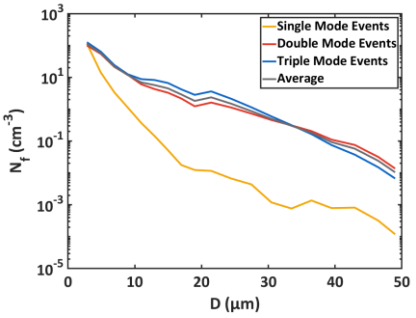

~~**Figure 1 Average spectrums of fog events with different modes**~~

3.2 Mode Transitions and Possible Mechanisms

Figure 3 presents the temporal evolution of meteorological variables, visibility, microphysical properties, and droplet spectrum for the five selected cases. Surface, 850 hPa, and 700 hPa synoptic conditions preceding each fog event are provided in the Appendix. MODIS 3.9 μm shortwave infrared and visible channel imagery for F1-1, F10, and F20 are provided in the appendix (Figures A2-A4). For F4 and F22, no satellite imagery is available within the fog period because the overpass times of the polar-orbiting satellite did not coincide with the observations. Fog Case 22 is a unimodal event with a short duration and discontinuity in time. Fog Case 4 is a bimodal event with a distinct formation-dissipation lifecycle lasting for approximately 3 hours. Fog Cases 1-1, 10 and 20 are all trimodal events. Fog Cases 1-1 and Fog Cases 10 both lasted over 12 hours but showed distinct lifecycle characteristics, whereas Fog Case 20 formed during daytime and experienced two clear formation and dissipation cycles. The maximum LWC used as an indicator of mature phase is marked in Figure 4, 5, 6, 7, 8.

~~To address these questions and further investigate the fog lifecycle as well as underlying physical mechanisms of different modes exhibit in DSDs, four representative cases were selected to analyze the temporal evolution of microphysical properties. Case 6 is a unimodal event with a short duration and discontinuity in time. Case 12 is a bimodal event with a distinct formation-dissipation lifecycle lasting for approximately 2.5 hours. Cases 1-1 and 10 are both trimodal, lasting over 12 hours but displaying different lifecycle characteristics. The maximum LWC used as an indicator of mature phase is marked in Figure 2.~~

~~For Fog Case 6 (F6), N_f and LWC vary intensely and discontinuously at 1-minute resolution, while FBS remains relatively high. The unimodal DSDs in F6 is relatively narrow, with correspondingly small R_v and R_{eff}, indicating that condensational growth was limited after fog droplet activation.~~

Fog Case 22 (F22) was a radiation-advection fog event. Under nocturnal radiative cooling on a clear night, surface temperature decreased and light fog formed around 2018/11/28 06:00. Weak warm, moist advection at 850 hPa further supported its development and persistence (Figure A6). At fog onset, visibility decreased sharply. After LWC reached its maximum, visibility and temperature gradually increased, and around 09:00 the rising wind speed and shifting wind direction accelerated the fog dissipation. It exhibiting relatively low N_f and LWC, while FBS remains higher than 60%. The N_f increases slowly before the LWC reaches its maximum, then gradually decreases as visibility and temperature rise, indicating a slow dissipation of fog. The DSD remains unimodal throughout, with small droplets contributing most of the N_f (Figure 4).

~~Fog Case 12 (F12) shows a clear formation-dissipation evolution: before LWC reaches its maximum, N_f and LWC continue to increase, followed by a gradual decrease after maximum LWC. R_v, R_{eff} and dispersion are positively correlated with LWC, while FBS shows a negative correlation. The DSD become bimodal (3,21 μm) in only 15 minutes after fog formation. As fog develops, N_f across all droplet sizes increases rapidly while the DSDs remain bimodal, indicating active condensational growth of droplets. After reaching the maximum LWC, N_f decreases accompanied by a mode transition from bimodal to unimodal as the fog dissipates. This may suggest that droplet activation/condensation and deactivation/evaporation occur simultaneously during fog evolution.~~

Fog Case 4 (F4) is an advection fog event. Under the influence of a high-pressure ridge, the lower atmosphere was stable with weak winds. Warm, moist air at 850 hPa was advected over a colder surface, cooled to near-saturation, and condensed to form fog (Figure A7). It shows a clear formation-dissipation evolution. About 40 minutes after fog formation, visibility gradually decreased as N_f and LWC increased. Temperature initially decreased and then rose, with the lower temperatures during the formation and development stages favoring fog lasting. As temperature increased, visibility also rose, and the fog slowly dissipated. Before LWC reaches its maximum, N_f and LWC continue to increase, followed by a gradual decrease after maximum LWC. R_v, R_{eff} and dispersion are positively correlated with LWC, while FBS shows a negative correlation. At the beginning of fog formation, the DSD was trimodal. As the fog developed, the N_f of 10-20 μm droplets increased rapidly, and the DSD shifted to a bimodal form with a dominant peak near 13 μm. During fog dissipation, the double mode persisted, with N_f gradually decreasing across all size ranges (Figure 5).

~~The average N_f and LWC of F6 and F12 are 167.97, 168.93 cm^{-3} and 0.01, 0.02 g m^{-3} respectively, which is comparable. However, the DSD is initially unimodal and remains unimodal throughout fog development, whereas F12 exhibits a broader, initially bimodal distribution. The observation site is surrounded by industrial facilities, leading to pronounced diurnal variation in aerosol concentration. Since the initial DSD is primarily affected by environmental supersaturation and aerosol chemical properties (Mazoyer et al., 2022), this may indicate that because F12 formed around midday, it was influenced by industrial emissions, resulting in the presence of more hygroscopic aerosols serving as CCN. Meanwhile, such a polluted background likely introduces larger aerosols and a broader aerosol size distribution, resulting in a wider initial DSD.~~

Fog Case 1 was a radiation-advection fog event lasting 39 hours. It formed under radiative cooling conditions, with sustained southwest warm and moist airflow supporting its long duration (Figure A8). To enable a clearer and more detailed analysis of its microphysical characteristics, the event was divided into two events at approximately the 14th hour after fog formation, based on the temporal evolution of N_f and LWC. The exact initial and end times of these two events, as well as their positions within the full fog lifecycle (F1), are provided in Table A1 and Figure A2 of the Appendix.

~~Fog Case 1 persisted for approximately 39 hours, to enable a clearer and more detailed analysis of its microphysical characteristics, the event was divided into two events at approximately the 14th hour after fog formation, based on the temporal evolution of N_f and LWC. The exact initial and end times of these two events, as well as their positions within the full fog lifecycle (F1), are provided in Table A1 and Figure A1 of the Appendix.~~

In Fog Case 1-1 (F1-1), visibility dropped sharply, accompanied by rapid increases in N_f and LWC. After LWC reached its maximum, temperature continued to decrease slowly, while wind direction remained steady and wind speed increased slightly, conditions that helped sustain the fog. The N_f and LWC of F1-1 are 352.38 cm^{-3} and 0.27 g m^{-3} respectively, significantly higher than those of F10 (229.53 cm^{-3} and 0.06 g m^{-3}).~~The N_f and LWC of F1-1 are 351.56 cm^{-3} and 0.27 g m^{-3} respectively, significantly higher than those of F10 (231.02 cm^{-3} and 0.06 g m^{-3}).~~ which may be attributed to differences in their lifecycle characteristics. F1-1 experienced a rapid development after formation, with N_f sharply increasing to approximately 600 cm^{-3}

within one hour. Following the drastic intensification there is a relatively stable phase lasting about 11 hours before gradual dissipation, during which the N_f and LWC remain relatively high.

As the fog continued to develop, N_f in the 5-20 μm range decreased, while those above 20 μm increased rapidly, and the DSD gradually transitioned from trimodal to bimodal, suggesting a mass transfer from smaller to larger droplets as the DSD broadens toward larger droplets (Figure 7).

~~Fog Case 10 (F10) maintains stable with relatively low N_f and LWC for the first 6 hours then experiences several pronounced fluctuations before dissipation. This difference in lifecycle also leads to distinct DSD evolution. In F10, the N_f across all sizes increases gradually and the DSDs becomes trimodal less than one hour before the time LWC reaches its maximum. Subsequently, due to significant fluctuations in N_f, the DSD varies accordingly, transitioning from trimodal to bimodal and eventually to unimodal. In contrast, the rapid developments in F1-1 results in a sharp increase in N_f, with DSDs becoming trimodal directly from unimodal within 2 hours after fog formation, instead of experiencing a bimodal stage like F10.~~

Fog Case 10 (F10) formed as a radiation fog under high-pressure control and weak surface winds (Figure A9). and remained stable with relatively low N_f and LWC for the first 6 hours. After 2007/12/20 06:00, rising temperature and variable wind direction enhanced turbulent mixing and promoted fog development. N_f and LWC increased with pronounced fluctuations, which were also reflected in the evolution of the DSD. Both R_v and R_{eff} increased with fluctuations, corresponding to the marked increase in N_f of droplets larger than 20 μm as shown by the DSD (Figure 8).

Fog Case 20 (F20) is an advection fog event. Under high-pressure control, easterly and southeasterly winds transported warm, moist marine air over a cold surface cooled by nocturnal radiative loss, providing favorable conditions for fog formation (Figure A10). This event featured relatively low N_f and LWC, with stable temperature and wind direction as well as wind speeds below 3 m s^{-1}, conditions conducive to fog maintenance. The DSDs were predominantly trimodal, with a marked decrease in the N_f of droplets larger than 7 μm, and the FBS remained consistently high at above 60% (Figure 9).

It should be noted that F4, F1-1 and F10 all exhibited a transition from trimodal to bimodal DSDs as the fog intensified, though with varying peak diameters. F10 and F4 had similar mean N_f, but F10 showed a higher FBS. Stronger condensational competition among small droplets in F10 led to more uniform particle sizes, suppressing further growth and resulting in a smaller peak diameter (11 μm) compared to F4 (13 μm). In F1-1, continuous transport of warm, moist air from the ocean sustained high N_f and LWC over an extended period of time, producing DSDs with larger peak diameters (3, 15, and 23 μm).

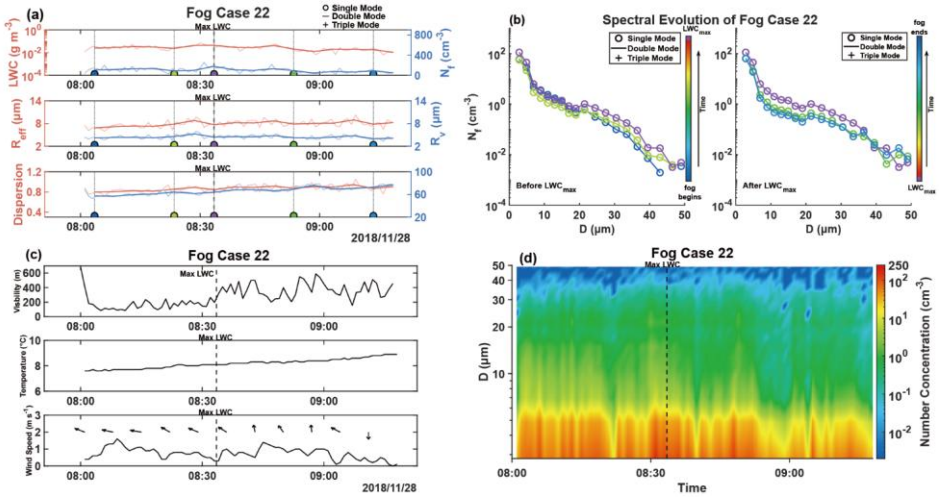

Figure 4 (a) is the temporal evolution of N_f, LWC, R_v, R_{eff}, FBS and dispersion for fog case 22, the dark lines represent 5-minute averaged values while the light lines are 1-minute averaged values. (b) is the 5-minute average DSD. As LWC reaches its maximum, the colors vary from blue to red, and each DSD in (b) are marked by colored dots in (a) with each color corresponding to a specific DSD and its number of peaks indicated. (c) is the temporal evolution of visibility, temperature and wind speed, with wind direction represented by wind barbs. (d) is the 1-minute temporal evolution of DSDs.

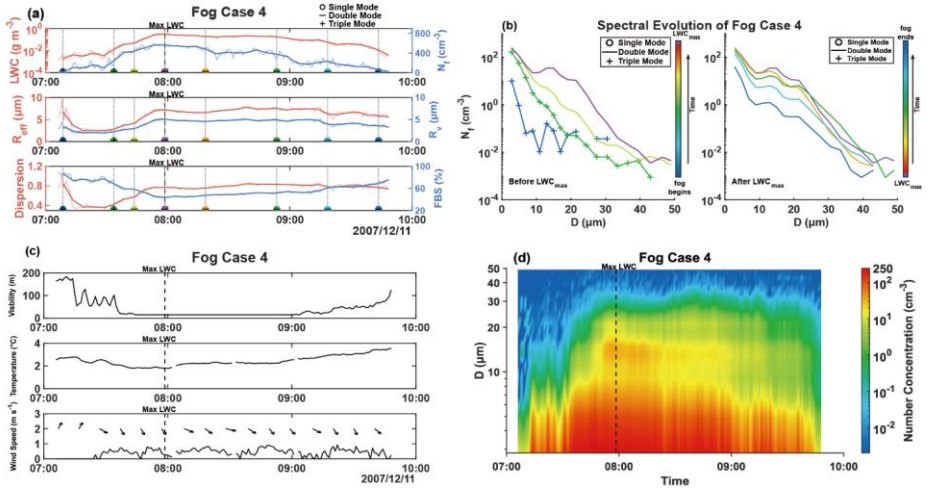

Figure 5 Time series of microphysical variables, DSDs, and meteorological elements for fog case 4.

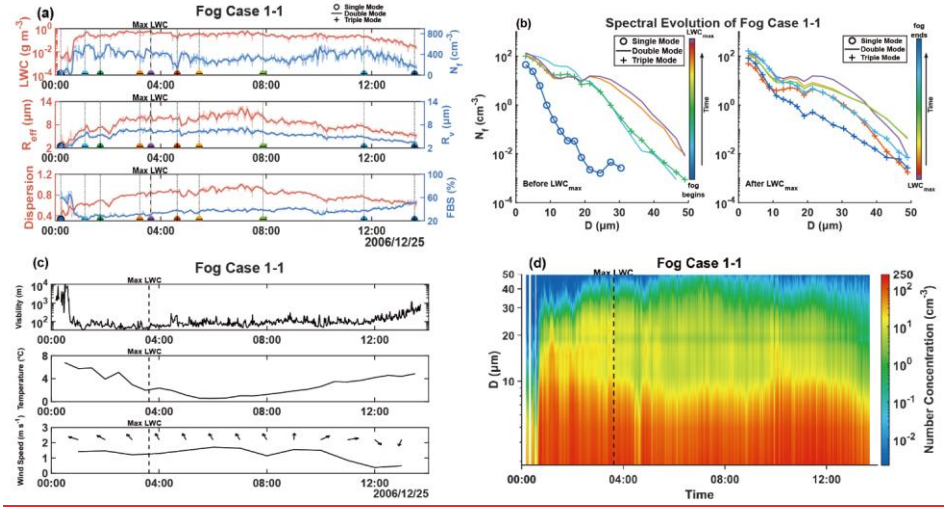

Figure 6 Time series of microphysical variables, DSDs, and meteorological elements for fog case 1-1.

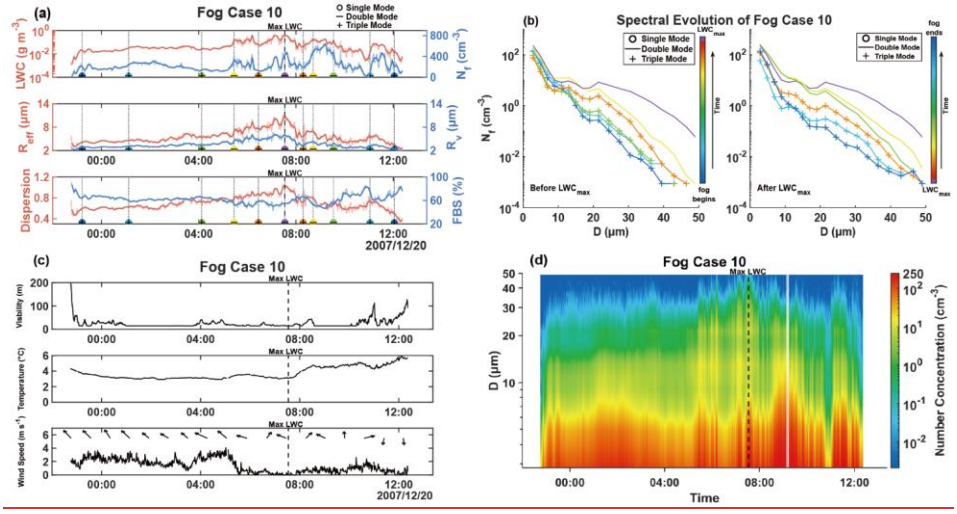

Figure 7 Time series of microphysical variables, DSDs, and meteorological elements for fog case 10.

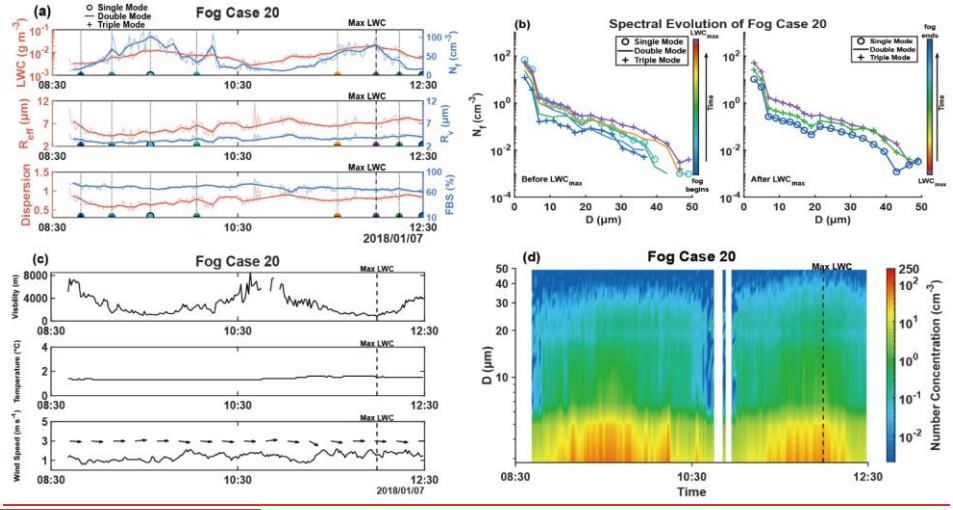

Figure 8 Time series of microphysical variables, DSDs, and meteorological elements for fog case 20.

360

设置了格式: 英语(美国)

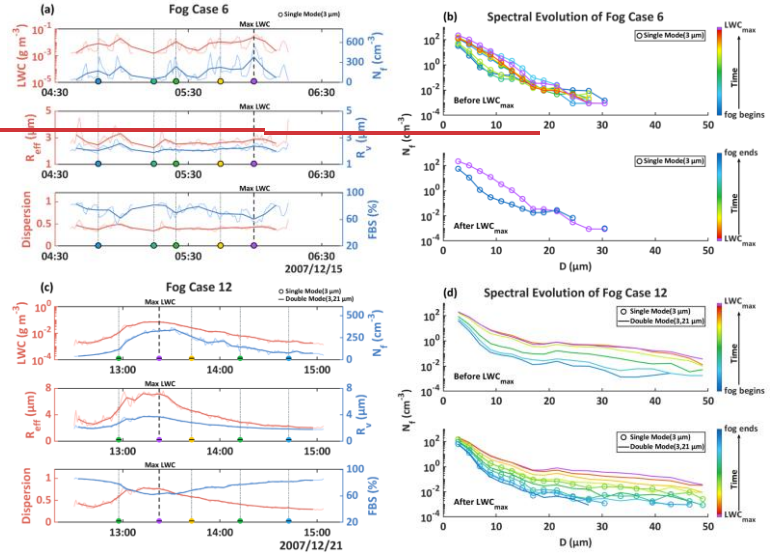

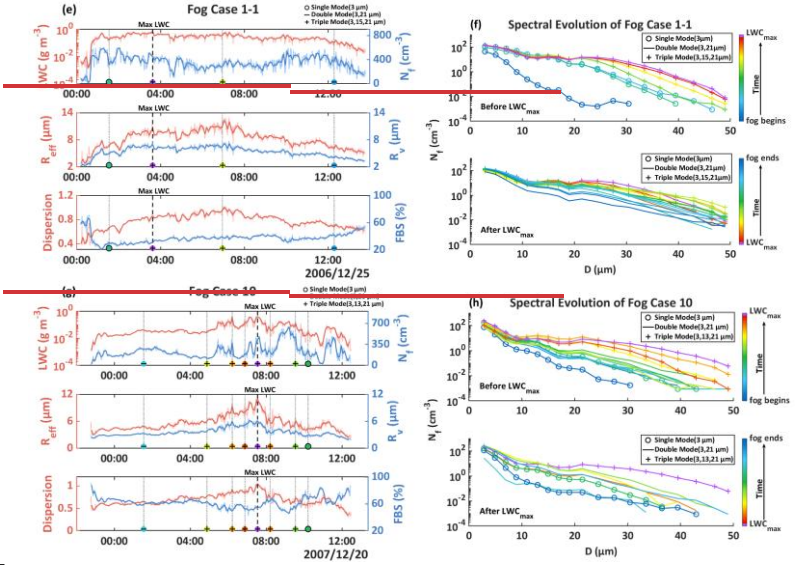

365 **~~Figure 2 (a), (c), (e), (g) are the temporal evolution of N_t, LWC, R_v, R_{eff}, FBS and dispersion for fog case 6, 12, 1-1, 10, the dark lines represent 5-minute averaged values while the light lines are 1-minute averaged values. (b), (d), (f), (h) are the 5-minute average DSD for case 6, 12, 1-1, 10. As LWC reaches its maximum, the colors vary from blue to red in (b), (d), (f), (h). The DSDs in (b), (d) are plotted every 10 minutes, while those in (f), (h) are plotted every 40 minutes. A part of DSDs is marked by colored dots in (a), (c), (e), (g). The positions of dots show time of each DSD and colors correspond to those in (b), (d), (f), (h).~~**

370

~~Note that around the time LWC reaches its maximum, both F1-1 and F10 exhibit a decrease in N_T within the 10-30 μm range and an increase above 30 μm. During this period, increases in R_v and R_{eff} are observed in both cases, suggesting a mass transfer from smaller to larger droplets as the DSD broadens toward larger droplets. However, a slight increase in total N_T and FBS is also noted simultaneously. This may suggest that aerosol continues to be activated during condensational growth,~~

375 ~~leading to the formation of new small droplets.~~

~~A comparison between F12 and F10 reveals that the mode centered at 21 μm forms nearly simultaneously with the 3 μm mode, which is in agreement with findings from a semi-urban area of Paris (Mazoyer et al., 2022). Meanwhile, the third mode, centered around 13 μm, emerges only during the later stage of fog development, typically near the time LWC reaches its maximum, corresponding to the mature phase of the fog. This suggests that the mode centered at 13 μm likely requires~~

380 ~~sustained water vapor supply and supersaturation, whereas the other two modes are more strongly influenced by initial environmental supersaturation and aerosol properties.~~

3.3 Correlation of modes and microphysical properties

Figure 9~~3~~ presents the probability distributions of N_f and LWC across unimodal and multimodal DSDs. For all modal types, N_f are primarily below 750 cm^{-3}, with probability density functions (PDFs) decreasing as N_f increases. For double mode DSDs, N_f primarily ranges between 200 and 500 cm^{-3}, while for triple mode DSDs, it is concentrated below 250 cm^{-3} and above 400 cm^{-3}. The PDF of single mode DSDs declines most rapidly with increasing LWC. Triple mode DSDs exhibit the widest LWC range, but their PDF within 0.2-0.4 g m^{-3} is lower than that of double mode DSDs. For single mode DSDs, the PDF of R_v decreases continuously beyond 4 μm. In double mode DSDs, R_v primarily falls within 3-6 μm, while triple mode DSDs exhibit a bimodal pattern with higher frequencies in the 2-3 μm and 5-6 μm ranges. Regarding the PDF of R_{eff}, single mode DSDs show a narrower distribution, triple mode DSDs have higher PDF values within 4-6 μm, and double mode DSDs are mainly concentrated in the 5-7 μm range.

设置了格式: 英语(美国)

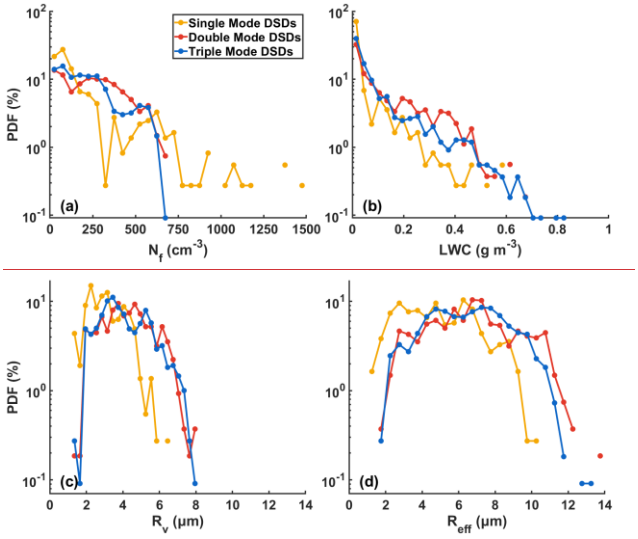

Figure 9 PDF distributions of N_f (a), LWC (b), R_v(c) and R_{eff} (d) for DSDs with different modes

~~The PDF decreases with increasing LWC, except for the trimodal case showing an increasing trend when LWC < 0.1 g m^{-3}. The PDF of unimodal DSDs exhibit the strongest decline and the narrowest distribution range. In the trimodal DSDs, LWC is more likely to reach higher than 0.2 g m^{-3}, while the PDF in the LWC < 0.2 g m^{-3} range is lower than those of unimodal and bimodal DSDs. For R_v and R_{eff}, unimodal DSDs are mainly associated with 2-4 μm and 2-6 μm ranges respectively. In bimodal DSDs, these ranges shift to 2-6 μm for R_v and 4-10 μm for R_{eff}. R_v is generally greater than 4 μm while R_{eff} is greater than 6 μm in trimodal DSDs.~~

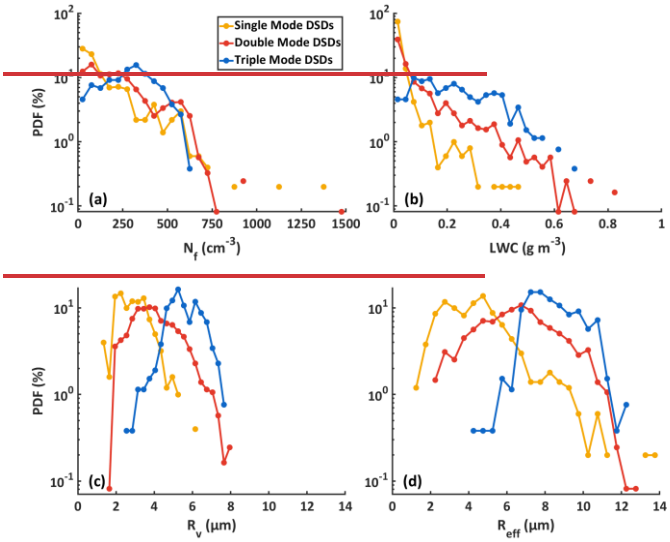

~~Figure 3 PDF distributions of N_t (a), LWC (b), R_v (c) and R_{eff} (d) for DSDs with different modes~~

Figure 1~~0~~4 shows the contributions of each droplet size bin to total N_f and LWC with different modal. The contribution of each bin to N_f aligns well with the number of modes. For unimodal DSDs, contributions to N_f decrease monotonically with increasing droplet diameter.

Compared to unimodal DSDs, the decrease in contribution to N_f with increasing droplet size is slower in multimodal cases. In particular, large droplets contribute more to N_f in trimodal DSDs than in bimodal ones, especially in the 18-26 μm range, which corresponds to the peak diameters of the trimodal distributions. However, for unimodal DSDs, the droplet size bin contributing most to LWC is not the first one, despite its accounting for 55% of the total N_f, indicating that larger droplets contribute more significantly to LWC. In both bimodal and trimodal DSDs, the 20-23 μm bin contributes most to the LWC. In the trimodal DSD, the contribution from small droplets to LWC is significantly lower than in other DSDs, with the main contribution coming from droplets in the 14-32 μm range, showing a more concentrated distribution.

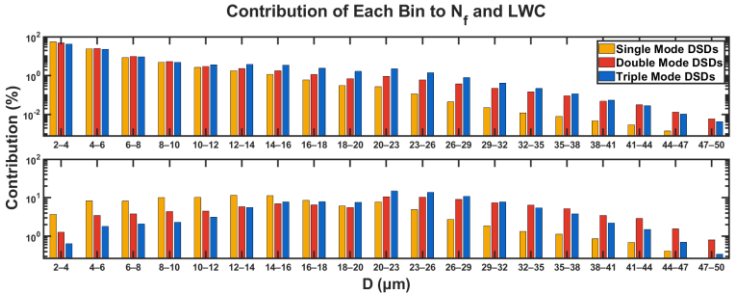

Figure 10 Contributions of each DSD bin to N_f and LWC with different modes

~~Compared to unimodal DSDs, bimodal and trimodal DSDs exhibit smaller FBS and greater contributions at the droplet sizes corresponding to their peaks, which are 20–23 μm for bimodal, 12–14 μm and 20–23 μm for trimodal DSDs. However, for unimodal DSDs, the droplet size bin contributing most to LWC is not the first one, despite its accounting for 55% of the total N_T, indicating that larger droplets contribute more significantly to LWC. In bimodal and trimodal DSDs, contributions of each bin to LWC first increase and then decrease with droplet diameter. The greatest contribution occurs at the 20–23 μm bin, which coincides with the second mode (21 μm). In trimodal DSDs, LWC is primarily contributed by droplets in the 12–32 μm range, showing a more concentrated distribution than in bimodal cases, likely due to the presence of the third mode around 11–15 μm.~~

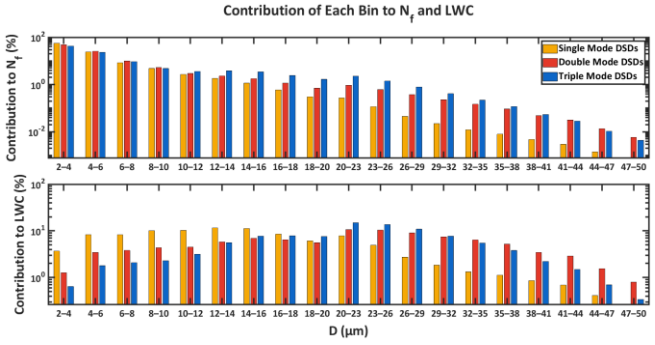

~~Figure 4 Contributions of each DSD bin to N_t and LWC with different modes~~

3.4 Performances and improvement of gamma and lognormal fitting~~Performances of gamma fitting and improvement~~

Bulk microphysical schemes commonly represent DSDs with gamma or lognormal distributions, making the accuracy of these representations critical to performance of numerical simulation. To evaluate the validity of the gamma and lognormal distribution for winter fog in Nanjing, mean DSDs of 27 observed fog events are fitted using the form of Eq. (11) and (12) with i=1. For the fog events examined in this study, both gamma and lognormal distribution provide a good fit to the average DSD in the small-droplet range (2-10 μm), but significantly underestimates number concentrations as droplet size increases, especially the gamma distribution. In multimodal DSDs of examined events, besides the peak mode near 3 μm, additional peaks are observed, which likely contribute to the poor fit. The probability distribution of peak mode diameters across all DSDs (Figure 10) indicates that the other two peaks are mainly concentrated around 10 μm and 22 μm. Therefore, segmented gamma and lognormal fitting was conducted using 10 μm and 22 μm as partition points (Figure 12b, c, e, f). When DSDs are segmented at 10 μm, the 2-10 μm range is well represented, but the fit increasingly underestimates number concentrations for diameters above 30 μm. When segmented at 22 μm, good agreement is achieved in the 2-10 μm and 22-50 μm ranges, but the 10-22 μm segment shows substantial deviation between the fitted and observed DSD. Based on these results, a three-segment gamma fitting approach was applied using 10 μm and 22 μm as partition points (Figure 12d, h). This approach significantly improves the overall fit ranging from 2 to 50 μm, providing a more accurate representation of the whole DSDs.

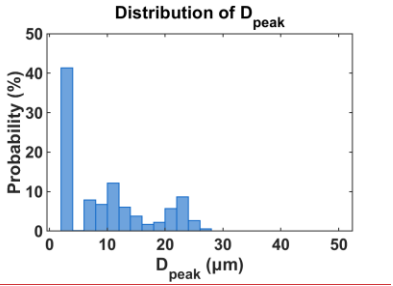

Figure 11 The probability distribution of peak mode diameters derived from lognormal fits to all DSDs

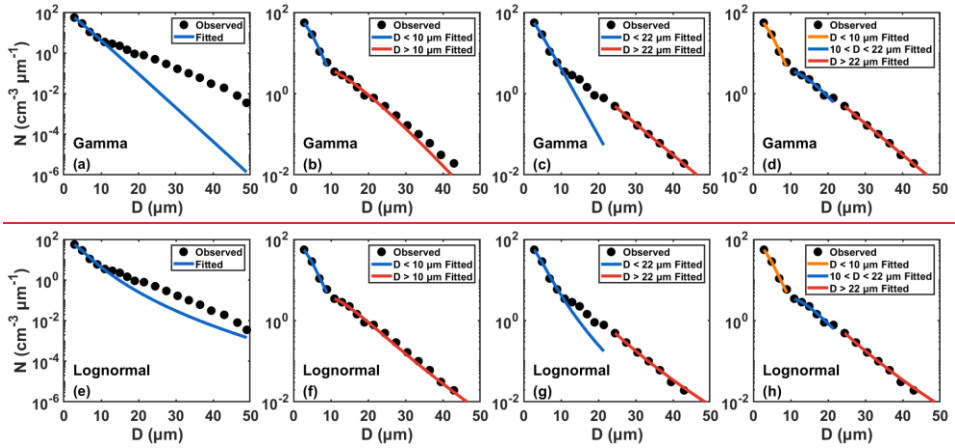

Figure 12 Gamma and lognormal fitting of the mean spectrum: original fit (a) (e), two-segment fitting with a breakpoint at 10 μm (b) (f), two-segment fitting with a breakpoint at 22 μm (c) (g), and three-segment fitting with breakpoints at 10 and 22 μm (d) (h).

To demonstrate that the superior performance of the three-segment gamma and lognormal fitting is due to the physically meaningful segmentation based on the characteristics of DSDs, rather than merely the increased number of segments, we evaluated the performance of alternative segmented fitting. Since the gamma and lognormal distributions are nonlinear, two fitting points would fall on a straight line and cannot uniquely constrain the curvature of the distribution, potentially leading to non-identifiable or ill-posed parameter estimates. Therefore, the segmentation points must satisfy two conditions: the full spectrum must be divided into three segments, and each segment must contain at least three bins. Under these constraints, 66 feasible segmentation combinations exist. Using each set of segmentation points, we performed gamma and lognormal fits for all DSDs and retrieved the corresponding N_t, LWC, R_v, and R_{eff}. The absolute deviations between the retrieved values and the observed ones were compared for both the alternative fittings and the fixed 10 μm and 22 μm segmentation (Figure 13). For all four microphysical parameters, the deviations from the fixed-segmentation fitting are significantly smaller than those from alternative segmentation. A two-sided binomial test was conducted to evaluate the probability that the fixed segmentation outperforms the alternative segmentation. For both distributions, the 95% confidence interval is [0.986, 1.000] with a p-value of 2.23e-308. These p-values are far below the 0.05 significance threshold. These results confirm the effectiveness of the 10 μm and 22 μm segmentation for both gamma and lognormal distribution.

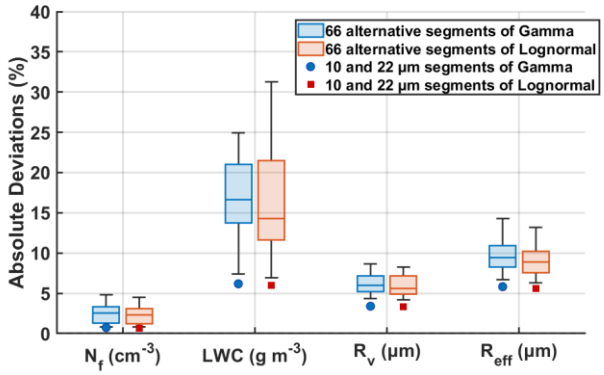

Figure 13 Boxplots of the mean absolute deviations from 66 alternative segmented fittings, with red dots indicating the mean deviations from the fixed 10 μm and 22 μm segmentation

To further evaluate the performance of the gamma and lognormal fitting with different breaking points, N_f, LWC, R_v, and R_{eff} were calculated based on both the original fit and segmented fit, and compared with those derived from observations. The deviation distribution between fitted and observed results are analysed in Figure 13, and the correlation between them are showed in Figure A11. The non-segmented gamma fit significantly underestimates the N_f of droplets larger than 10 μm, leading to underestimation of all derived microphysical quantities. The N_f calculated from the two-segment fit with a breakpoint at 10 μm is close to observation, but the derived LWC are still underestimated. For the fit segmented at 22 μm all microphysical quantities are underestimated, likely due to underrepresentation of droplet concentrations in the 10-22 μm range. Compared to the non-segmented gamma fit approach, the three-segment fitting shows substantial improvement in the high N_f regime (N_f > 700 cm^{-3}) and in LWC estimation as the results are tightly clustered around the zero-deviation line and the 1:1 line. Also, the fitting accuracy for R_{eff} and R_v is also improved for both gamma and lognormal fitting.

Except for the non-segmented gamma fitting, the other three segmented approaches exhibit a clear pattern in estimating R_{eff}: underestimation primarily occurs when the observed R_{eff} < 6 μm, while overestimation tends to occur when the observed R_{eff} > 6 μm (Figure A11). This pattern is particularly pronounced in the fitting segmented at 22 μm, whereas the three-segment fitting shows notable improvement in reducing underestimation at lower R_{eff} values.

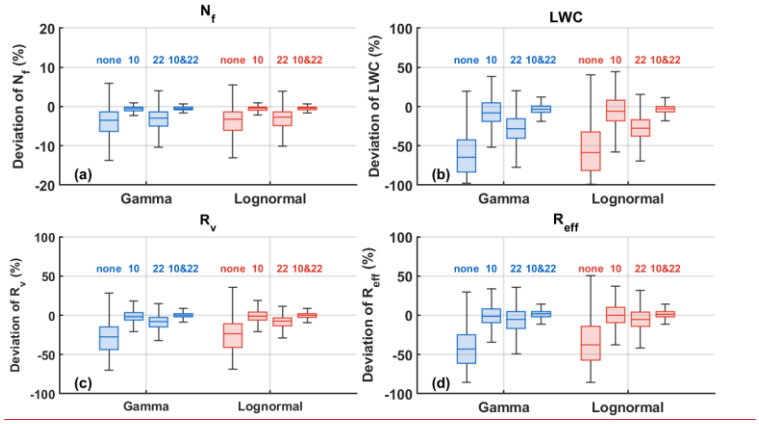

Figure 14 Deviation distribution of N_f, LWC, R_v and R_{eff} between observation spectrum and the gamma and lognormal fitted spectrum. The number above each boxplot indicates the segmentation position (μm); 'none' denotes no segmentation point applied.

In bulk microphysical schemes, the gamma distribution is commonly used to represent DSDs, making the accuracy of this representation critical to simulation performance. To evaluate the validity of the gamma distribution for winter fog in Nanjing, mean DSDs of 31 observed fog events are fitted by

$$n(D) = N_0 D^{\mu} e^{-\lambda D} \quad (9)$$

where D is the droplet diameter, $n(D)$ is the number concentration for each bin, N_0, μ and λ are three distribution parameters. The fitting results are shown in Figure 5.

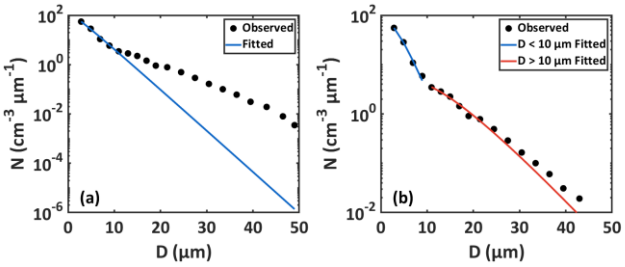

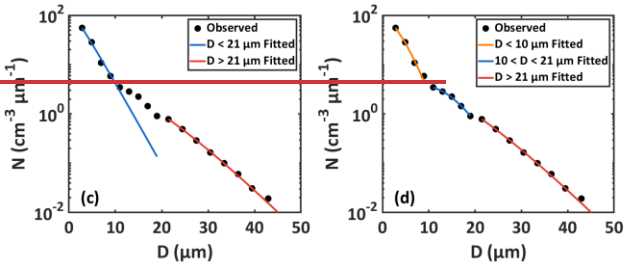

Figure 5 Gamma fitting of the mean spectrum: original fit (a), two-segment fitting with a breakpoint at 10 μm (b), two-segment fitting with a breakpoint at 21μm (c), and three-segment fitting with breakpoints at 10 and 21 μm (d).

For the fog events examined in this study, the gamma distribution provides a good fit to the average DSD in the small-droplet range (2-10 μm), but significantly underestimates number concentrations as droplet size increases. In multimodal DSDs of examined events, besides the peak near 3 μm, additional peaks are observed around 10 μm and 21 μm, which likely contribute to the poor fit. To address this, segmented gamma fitting was conducted using 10 μm and 21 μm as partition points. When DSDs are segmented at 10 μm, the 2-10 μm range is well represented, but the fit increasingly underestimates number concentrations for diameters above 30 μm. When segmented at 21 μm, good agreement is achieved in the 2-10 μm and 20-50 μm ranges, but the 10-20 μm segment shows substantial deviation between the fitted and observed DSD.

Based on these results, a three-segment gamma fitting approach was applied using 10 μm and 21 μm as partition points (Figure 5d). This approach significantly improves the overall fit ranging from 2 to 50 μm, providing a more accurate representation of the whole DSDs.

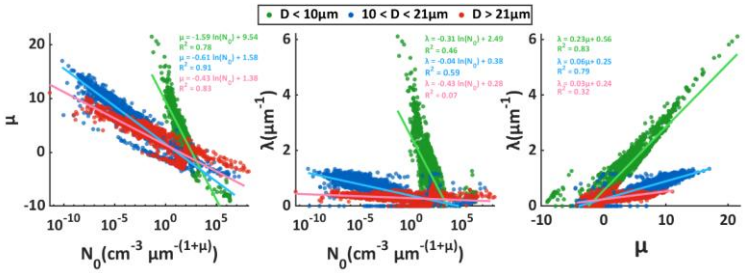

Figure 6 Correlation between the N_0, μ and λ derived from the three-segment gamma fitting

The interrelationships among the three fitting parameters obtained from the three-segment gamma fitting are shown in Figure 6. For each segment, N_0 exhibits a negative correlation with both μ and λ, while μ and λ are positively correlated. In the D

~~< 10 μm segment, larger N_0 and λ are observed, indicating a narrower and more concentrated spectrum with a steep decline in number concentration as droplet size increases. For D > 10 μm, N_0 shows a wider distribution with smaller μ and λ, reflecting broader spectrum and higher number concentrations of larger droplets.~~

~~Compared to the D > 10 μm segments, N_0 in the D < 10 μm range is more tightly gathered in a range of 10^9-10^5 cm^{-3} $\mu m^{-(1+\mu)}$, suggesting that small droplet concentrations are higher and more consistent across different DSDs. This may indicate that environmental supersaturation is consistently sufficient to activate aerosols. However, the continued growth of activated droplets via condensation depends on the persistence of supersaturation under vapor consumption.~~

Cloud optical thickness (τ) and single-scattering albedo (ω_0) are key parameters for evaluating the Twomey effect (Stephens, 1984; Twomey and Bohren, 1980). τ can be calculated with

$$\tau = \int \frac{3LWC}{D_{eff}} dz \quad (16)$$

where z is the thickness of the cloud or fog layer (Stephens, 1978). When assuming cloud or fog is vertically homogeneous, Eq. (14) can be simplified as

$$\frac{\tau}{dz} = \frac{3LWC}{D_{eff}} \quad (17)$$

where $\frac{\tau}{dz}$ represents the average optical thickness per layer. The single-scattering albedo (ω_0) can be expressed by

$$1 - \omega_0 = 1.7 k_w R_{eff} \quad (18)$$

where k_w is the complex part of the refractive index of water. Eq. (16) indicates the critical role of R_{eff} in the Twomey effect (Wang et al., 2019).

To more precisely assess the potential climate impact of inaccuracy in R_{eff} estimates from gamma and lognormal fitting, Eq. (17) and (18) were used to calculate absorption coefficient and optical thickness based on both observed and fitted R_{eff}. This allowed evaluation of the extent to which gamma and lognormal fitting overestimates or underestimates these parameters. Results are showed in Figure 15.

Due to its significant underestimation of N_f above 10 μm, the non-segmented gamma and lognormal fitting notably underestimates absorption coefficient ($1 - \omega_0$) and optical thickness (τ) by up to nearly 90%. Compared to the fitting segmented at 22 μm, the fitting segmented at 10 μm more accurately captures absorption coefficient and optical thickness, yet still exhibits up to 50% overestimation or underestimation of absorption coefficient. It is noteworthy that the 22 μm-segmented fitting generally underestimates optical thickness, likely due to the underestimation of N_f for droplets in the 10-22 μm range. In contrast, the three-segment fitting significantly improves the estimation of both absorption coefficient and optical thickness, with most deviations confined within ±20%. The most notable improvements lie in reducing the underestimation of absorption coefficient and the overestimation of optical thickness.

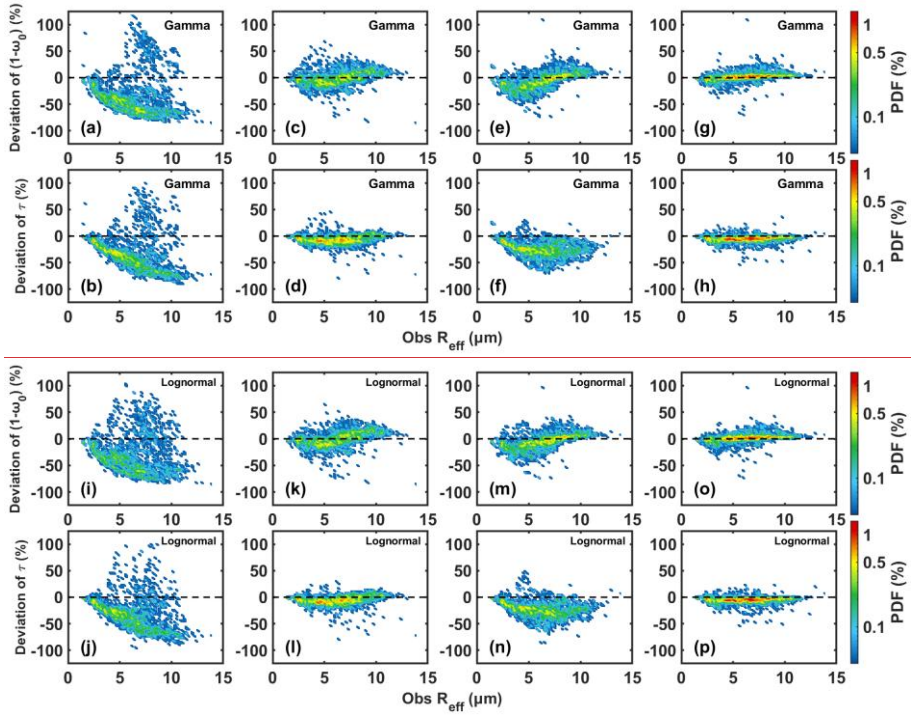

Figure 15 Correlation between absorption coefficient ($1-\omega_0$) and optical thickness (τ) derived from observed spectrum and those computed from the gamma-fitted spectrum with no breakpoint (a, b), breakpoint at 10 μm (c, d), breakpoint at 22 μm (e, f) and breakpoint at 10 μm and 22 μm (g, h).

~~To further evaluate the performance of the gamma fitting with different breaking points, N_f, LWC, R_{ψ}, and R_{eff} were calculated based on both the original fit and segmented fit, and compared with those derived from observations. The correlations between fitted and observed results are analyzed in Figure 7. As shown, the non-segmented gamma fit significantly underestimates the N_f of droplets larger than 10 μm, leading to underestimation of all derived microphysical quantities. These values are scattered around the 1:1 line, indicating poor agreement with observations. The N_f calculated from the two-segment fit with a breakpoint at 10 μm is close to observation, but the derived LWC and R_{ψ} are slightly overestimated. For the fit segmented at 21 μm both N_f and LWC are underestimated, likely due to underrepresentation of droplet concentrations in the 10-21 μm range. Compared to the non-segmented gamma fit approach, the three-segment fitting shows substantial~~

improvement in the high N_f regime (N_f > 700 cm^{-3}) and in LWC estimation as the results converge tightly around the 1:1 line. Also, the fitting accuracy for R_{eff} and R_v is also improved.

Except for the non-segmented gamma fitting, the other three segmented approaches exhibit a clear pattern in estimating R_{eff}: underestimation primarily occurs when the observed R_{eff} < 6 μm, while overestimation tends to occur when the observed R_{eff} > 6 μm. This pattern is particularly pronounced in the fitting segmented at 21 μm, whereas the three-segment fitting shows notable improvement in reducing underestimation at lower R_{eff} values.

Cloud optical thickness (τ) and single-scattering albedo (ω_0) are key parameters for evaluating the Twomey effect (Stephens, 1984; Twomey and Bohren, 1980). τ can be calculated with

$$\tau = \int \frac{3LWC}{D_{eff}} dz \quad (10)$$

where z is the thickness of the cloud or fog layer (Stephens, 1978). When assuming cloud or fog is vertically homogeneous, Eq. (9) can be simplified as

$$\frac{\tau}{z} = \frac{3LWC}{D_{eff}} \quad (11)$$

where $\frac{\tau}{z}$ represents the average optical thickness per layer. The single-scattering albedo (ω_0) can be expressed by

$$1 - \omega_0 = 1.7 k_w R_{eff} \quad (12)$$

where k_w is the complex part of the refractive index of water. Eq. (11) indicates the critical role of R_{eff} in the Twomey effect (Wang et al., 2019).

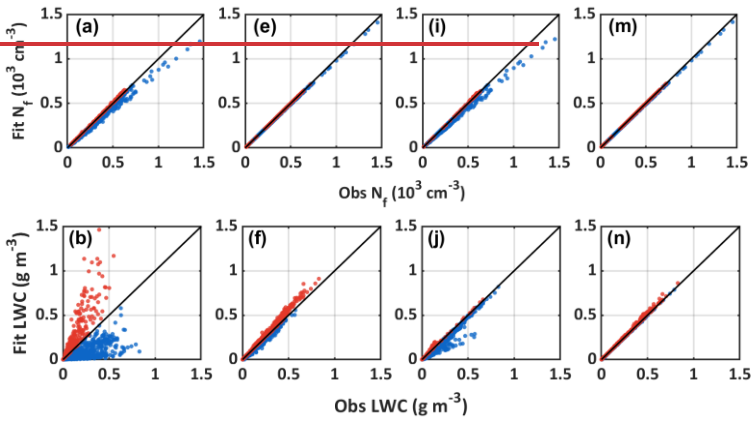

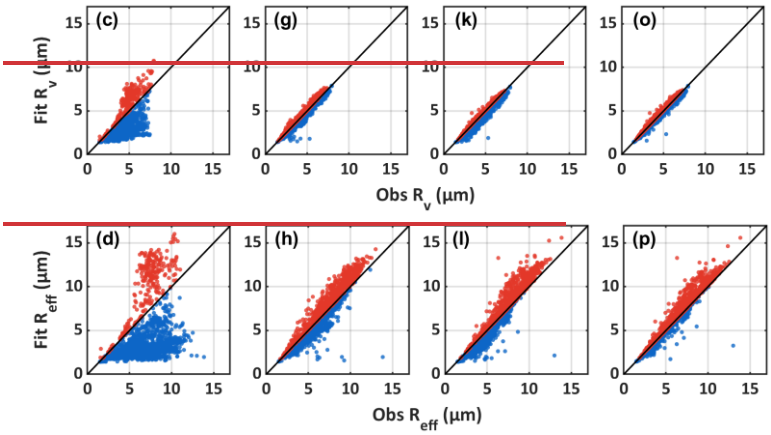

~~**Figure 7 Correlation between N_t, LWC, R_v and R_{eff} derived from observed spectrum and those computed from the gamma-fitted spectrum with no breakpoint (a-d), breakpoint at 10 μm (e-h), breakpoint at 21 μm (i-l) and breakpoint at 10 μm and 21 μm (m-p). Red dots indicate overestimation of the microphysical properties by the gamma fit, while blue dots indicate underestimation.**~~

~~To more precisely assess the potential climate impact of inaccuracy in R_{eff} estimates from gamma fitting, Eq. (11) and (12) were used to calculate absorption coefficient and optical thickness based on both observed and fitted R_{eff}. This allowed evaluation of the extent to which gamma fitting overestimates or underestimates these parameters. Results are showed in Figure 8.~~

~~Due to its significant underestimation of N_t above 10 μm, the non-segmented gamma fitting notably underestimates absorption coefficient ($1 - \omega_a$) and optical thickness (τ) by up to nearly 90%. Compared to the gamma fitting segmented at 21 μm, the fitting segmented at 10 μm more accurately captures absorption coefficient and optical thickness, yet still exhibits up to 50% overestimation or underestimation of absorption coefficient. It is noteworthy that the 21 μm-segmented fitting generally underestimates optical thickness, likely due to the underestimation of N_t for droplets in the 10-21 μm range.~~

~~In contrast, the three-segment gamma fitting significantly improves the estimation of both absorption coefficient and optical thickness, with most deviations confined within ±20%. The most notable improvements lie in reducing the underestimation of absorption coefficient and the overestimation of optical thickness.~~

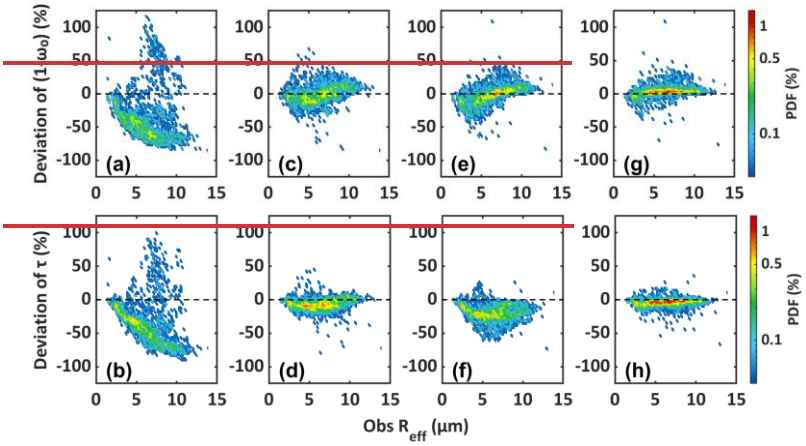

~~**Figure 8 Correlation between absorption coefficient ($1-\omega_0$) and optical thickness (τ) derived from observed spectrum and those computed from the gamma-fitted spectrum with no breakpoint (a, b), breakpoint at 10 μm (c, d), breakpoint at 21 μm (e, f) and breakpoint at 10 μm and 21 μm (g, h).**~~

The interrelationships among the three fittinpug parameters obtained from the three-segment gamma fitting are shown in Figure 16. For each segment, N_0 exhibits a negative correlation with both μ and λ, while μ and λ are positively correlated. In the D < 10 μm segment, larger N_0 and λ are observed, indicating a narrower and more concentrated spectrum with a steep decline in number concentration as droplet size increases. For D > 10 μm, N_0 shows a wider distribution with smaller μ and λ, reflecting broader spectrum and higher number concentrations of larger droplets.

Compared to the D > 10 μm segments, N_0 in the D < 10 μm range is more tightly gathered in a range of 10^0-10^5 cm^{-3} $\mu m^{-(1+\mu)}$, suggesting that small droplet concentrations are higher and more consistent across different DSDs. This may indicate that compared with droplets smaller than 10 μm, the formation of droplets larger than 10 μm is more affected by aerosol properties such as number concentration, size, and chemical composition, as well as by environmental factors including turbulence intensity, vertical motion, and spatiotemporal variations in supersaturation. Because the fitting parameters of lognormal distribution do not exhibit clear correlations, they are not shown here.

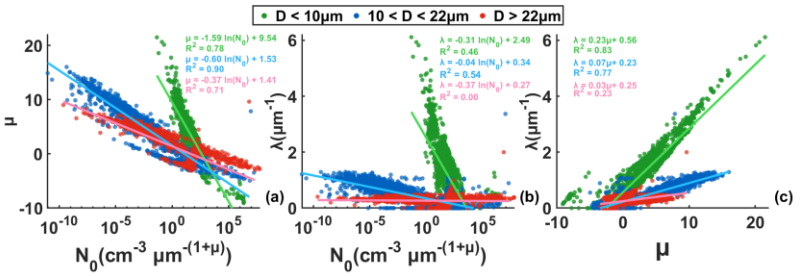

Figure 16 Correlation between the N_0, μ and λ derived from the three-segment gamma fitting

带格式的: 正文

~~4 Discussion~~

~~Numerous studies on fogs in Nanjing have primarily examined the influence of meteorological factors such as temperature, humidity, wind speed, and turbulence on fog evolution, investigated the correlations between microphysical properties, or compared microphysical properties of fogs in Nanjing with those in other regions (Ge et al., 2024; Liu et al., 2011; Lu et al., 2013; Niu et al., 2012), enhancing the scientific understanding of fog formation and dissipation in polluted urban backgrounds. However, current numerical models still struggle to accurately capture the evolution of fog lifecycles, partly due to the inadequate parameterization of fog DSDs. In bulk microphysical schemes, DSDs are described using predefined functions such as gamma distributions. However, previous studies have shown that DSDs vary significantly in time and space, deviating from the idealized functions (Khain et al., 2015; Nelli et al., 2024; Wang et al., 2021b).~~

~~Based on the analysis of fog droplet size distributions (2–50 μm) obtained from 27 winter fog events in 2006–2009 and 2017–2018 of Nanjing, China, unimodal, bimodal, and trimodal DSDs were identified across different fog events, as well as transitions among these modes within individual cases during fog development, stabilization, and dissipation. The three observed DSD modes peaking at 3 μm, 11–15 μm, and 21 μm are consistent with findings from both relatively clean background in Paris, France (Mazoyer et al., 2022) and polluted region in Jinan, China (Wang et al., 2021a). Due to the poor performance of gamma distribution in representing observed mean DSDs, segmented gamma fitting was conducted using 10 μm and 21 μm as partition points. The microphysical parameters derived from the segmented fits show markedly better agreement with observations, with particularly notable improvements from the three-segment fitting in the high regime of N_t and in LWC. Although the three-segment fitting still tends to underestimate R_{eff} when R_{eff} < 6 μm and overestimate it when R_{eff} > 6 μm, the deviations in retrieved R_{eff}, absorption coefficient and optical depth decreased substantially, from values up to 90% to around 20%.~~

4 Conclusions

~~5 Conclusions~~

As a key parameter of fog microphysical processes, the droplet size distribution (DSD) is influenced by multiple macro- and micro-scale factors, exhibits significant temporal and spatial variability, and evolves throughout the fog lifecycle, thereby posing challenges for accurate fog prediction (Niu et al., 2012; Nelli et al., 2024). Recent study has shown fog sensitivity to the shape of the DSD in models (Boutle et al., 2022). In microphysical schemes of numerical model,~~In bulk microphysical schemes,~~ the gamma and lognormal distribution is widely used to represent DSD, making its accuracy critical for reliable simulations.

This study investigates the microphysical characteristics of 27 winter fog events in Nanjing under polluted conditions, with a focus on the evolution of droplet size distributions (DSDs) throughout the fog lifecycle and on the application of segmented gamma fitting to the mean DSD for improved parameterization. The average N_f, LWC, R_v and R_{eff} vary over the ranges of 25-586 cm^{-3}, 0-0.27 g m^{-3}, 1.6-6 μm, 1.9-8.2 μm,~~The average N_f, LWC, R_v and R_{eff} vary over the ranges of 25-587 cm^{-3}, 0-0.28 g m^{-3}, 1.6-6 μm, 1.9-8.3 μm respectively,~~ which shows greater N_f, lower LWC and smaller droplets comparing to other clean regions such as the tropical rainforests of southwestern China (Wang et al., 2021~~b~~). Among the 27 fog cases, DSDs with single mode (3 μm), double mode (3, 7-13 μm) and triple mode (3, 9-15, 21-25 μm)~~single mode (3 μm), double mode (3, 21 μm) and triple mode (approximately 3, 13, 21 μm)~~ were observed. The main findings are as follows:

Among all fog cases, radiation fog accounts for the largest proportion. Radiation-advection fog tends to persist longer and is typically associated with trimodal DSDs. Unimodal cases are more likely to occur when the fog duration is short, the DSD is narrow, or the FBS is high. For bimodal and trimodal cases, both the number of peaks and their diameters vary with the fog life cycle. As the fog develops, sustained condensational growth often leads unimodal and trimodal DSDs to evolve into bimodal, with more concentrated peaks. The peak diameters are linked to the ability of fog to maintain high number concentrations and liquid water content. Although the N_f of larger droplets increases, droplets around 3 μm consistently exhibit the highest N_f, indicating continuous activation and formation of new droplets during the condensational growth.

~~Unimodal cases generally feature narrow DSDs with smaller N_f and LWC. In bimodal and trimodal events, the DSD evolves throughout the fog lifecycle: N_f increases and DSD broadens as fog develops while DSD transitioning from multimodal to unimodal during dissipation. The third mode (around 13 μm) typically emerges after the initial two (3, 21 μm) and appears near the time LWC reaches its maximum, suggesting that the formation of the third mode requires sustained water vapor supply and supersaturation. The underlying physical mechanisms and aerosol effects could be further investigated through sensitivity experiments using numerical modeling.~~

The probability density function (PDF) distributions of microphysical properties vary across spectral modes. For all modal types, the PDF decreases with increasing N_f and LWC.

Compared to trimodal DSDs, the PDF distributions of R_v and R_{eff} in bimodal DSDs are more concentrated. The contribution of each bin to N_f aligns well with the appearance of modes, while larger droplets contribute significantly to LWC.

~~Bimodal and multimodal DSDs are often associated with larger R_v and R_{eff}. The contribution of each bin to N_f aligns well with the appearance of modes, while larger droplets contribute significantly to LWC.~~

Comparison of the retrieved physical parameters from segmented gamma and lognormal fitting with observations indicates that the three-segment fitting yields the best performance, especially in improving N_f and LWC estimation. Meanwhile, the three-segment fitting reduces the estimation deviations in R_{eff}, absorption coefficient and optical thickness from up to 90% in the non-segmented fitting to below 20%, demonstrating its effectiveness in improving fog DSD representation and microphysical characteristic retrieval.

These findings advance our understanding of fog droplet size distribution (DSD) evolution during fog lifecycles and the correlations between DSD modes and microphysical properties, providing fundamental insights into fog microphysics in polluted urban regions such as the Yangtze River Delta, China. The improved segmented gamma and lognormal fitting offers a new perspective for DSD parameterization and demonstrates strong potential for improving the representation of cloud/fog microphysical processes in weather prediction and climate models.

It should also be noted that in this work, only a three-parameter~~two-parameter gamma~~ distribution was used to fit and refine the mean DSD. The comparative performance of alternative distribution and evaluate the influence of different parameterizations on fitting accuracy could be explored in future studies.

Appendix

A1 Details on the starting points and upper and lower bounds of parameters used for gamma and lognormal fitting

In this study, the DSDs were fitted using gamma distribution $n(D) = \sum_{i=1}^{3} n_i(D) = \sum_{i=1}^{3} N_{0,i} D^{\mu_i} e^{-\lambda_i D}$ and lognormal distribution $n(D) = \sum_{i=1}^{3} n_i(D) = \sum_{i=1}^{3} \frac{n_i}{2\pi^{1/2} D_i \ln\sigma_{g,i}} \exp\left(-\frac{(\ln D_i - \ln D_{g,i})^2}{2(\ln\sigma_{g,i})^2}\right)$ to determine the number of peaks and their peak diameters. Within the prescribed parameter bounds, nonlinear least squares were used to obtain the best solution for each value of i, and the optimal fit for a given DSD was selected from these solutions using AIC and BIC.

For gamma distribution, the same initial values and parameter bounds are applied for all values of i, and the optimal solution is obtained automatically during the fitting process. The initial values for the three parameters are [100, 1, 0.1], with lower bounds [0, −10, 0] and upper bounds [1000, 10, 10].

For lognormal distribution, three possible peak diameters (approximately 3 μm, 11 μm, and 21 μm) are identified based on the mean DSD of all cases (Figure A1). To minimize subjective influence, relatively broad bounds are assigned to the parameter D_g under different values of i, while keeping the same initial values. The bounds for D_g are 1-50 (i = 1), 1-50 and 5-50 (i = 2), and 1-50, 5-50, and 15-50 (i = 3). n and σ_g use unified bounds of 0-1000 and 1.05-5 regardless of i. The initial values for the parameters for all i are set to 100, 2, and 1.8.

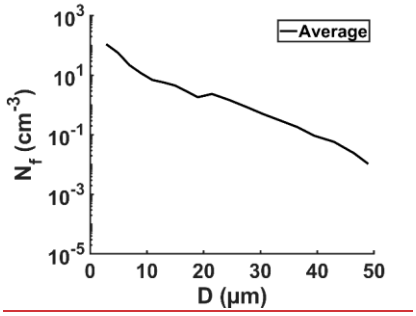

Figure A1 Average spectrums of all fog DSDs.

A2 Fog case classification and peak diameters at 1-min and 5-min resolution

Fog Case	Initial Time (local time)	End Time (local time)	Type	Modes (5-min Average)	Modes (1-min Average)
1-1	2006/12/25 00:10	2006/12/25 13:47	Radiation-advection	triple mode (3,15,23μm)	triple mode (3,15,23μm)

1-2	2006/12/25 13:48	2006/12/26 14:51	Radiation-advection	triple mode (3,7,13μm)	triple mode (3,7,13μm)
2	2006/12/26 17:46	2006/12/27 01:36	Radiation-advection	triple mode (3,9.25μm)	triple mode (3,9.25μm)
3	2006/12/27 03:28	2006/12/27 12:34	Radiation-advection	single mode (3μm)	single mode (3μm)
4	2007/12/11 07:06	2007/12/11 09:55	Advection	double mode (3,13μm)	double mode (3,13μm)
5	2007/12/14 05:38	2007/12/14 10:20	Radiation	double mode (3,13μm)	double mode (3,13μm)
6	2007/12/15 04:37	2007/12/15 06:15	Radiation	double mode (3,9μm)	double mode (3,9μm)
7	2007/12/15 07:06	2007/12/15 07:37	Radiation	single mode (3μm)	single mode (3μm)
8	2007/12/18 06:19	2007/12/18 10:35	Radiation	double mode (3,12μm)	double mode (3,13μm)
9	2007/12/19 00:23	2007/12/19 11:07	Radiation	double mode (3,11μm)	double mode (3,11μm)
10	2007/12/19 22:45	2007/12/20 12:28	Radiation	triple mode (3,11,21μm)	triple mode (3,11,21μm)
11	2007/12/21 03:39	2007/12/21 08:50	Radiation-advection	triple mode (3,11,23μm)	triple mode (3,11,21μm)
12	2007/12/21 12:30	2007/12/21 15:04	Advection	triple mode (3,11,23μm)	triple mode (3,11,23μm)
13	2007/12/21 16:30	2007/12/21 17:43	Radiation-advection	double mode (3,9μm)	triple mode (3,9,11μm)
14	2007/12/23 01:41	2007/12/23 05:05	Radiation	double mode (3,11μm)	double mode (3,11μm)
15	2008/12/04 21:03	2008/12/04 23:39	Radiation	single mode (3μm)	single mode (3μm)
16	2009/01/08 08:18	2009/01/08 12:08	Advection	triple mode (3,11,23μm)	triple mode (3,11,23μm)
17	2009/12/01 20:47	2009/12/02 10:42	Radiation	triple mode (3,11,23μm)	triple mode (3,11,23μm)
18	2017/12/31 05:10	2017/12/31 11:00	Radiation	single mode (3μm)	single mode (3μm)
19	2018/01/05 21:24	2018/01/05 23:48	Radiation	double mode (3,7μm)	double mode (3,7μm)
20	2018/01/07 08:41	2018/01/07 12:33	Advection	triple mode (3,9,25μm)	triple mode (3,9,25μm)
21	2018/11/26 20:47	2018/11/27 08:57	Radiation	triple mode (3,11,23μm)	triple mode (3,11,23μm)
22	2018/11/28 08:00	2018/11/28 09:22	Radiation-advection	single mode (3μm)	single mode (3μm)
23	2018/12/01 01:10	2018/12/01 08:08	Radiation-advection	triple mode (3,7,23μm)	triple mode (3,7,23μm)
24	2018/12/20 03:22	2018/12/20 08:05	Radiation	double mode (3,7μm)	double mode (3,9μm)
25	2019/01/04 21:49	2019/01/05 03:50	Radiation	single mode (3μm)	single mode (3μm)

26	2019/01/06 07:20	2019/01/06 08:39	Rain-induced	triple mode (3,9,25μm)	double mode (3,11,25μm)

Table A2 Fog case classification and peak diameters at 1-min and 5-min resolution

A3 MODIS 3.9 µm shortwave infrared and visible channel imagery for F1-1, F10, and F20

For F4 and F22, no satellite imagery is available within the fog period because the overpass times of the polar-orbiting satellite did not coincide with the observations.

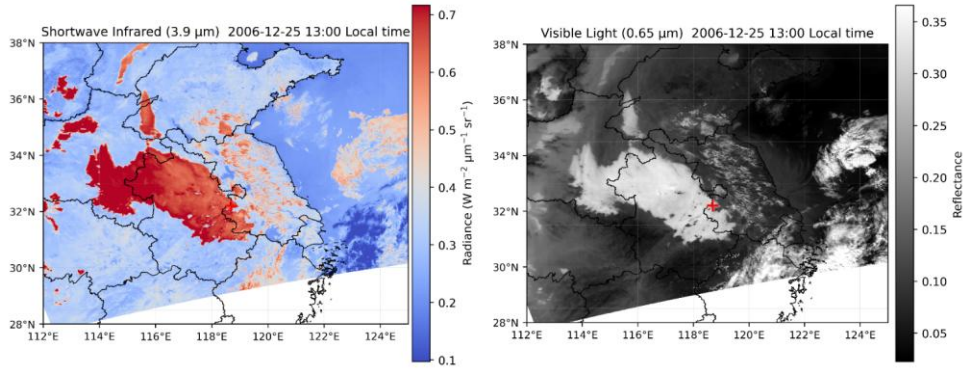

Figure A2 Aqua MODIS 3.9 µm shortwave infrared and visible channel imagery for Fog 1-1, with the observation site marked by a red cross.

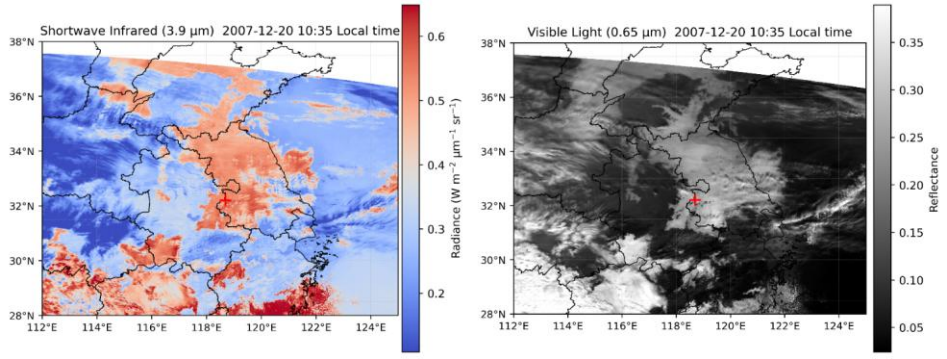

Figure A3 Terra MODIS 3.9 µm shortwave infrared and visible channel imagery for Fog 10, with the observation site marked by a red cross.

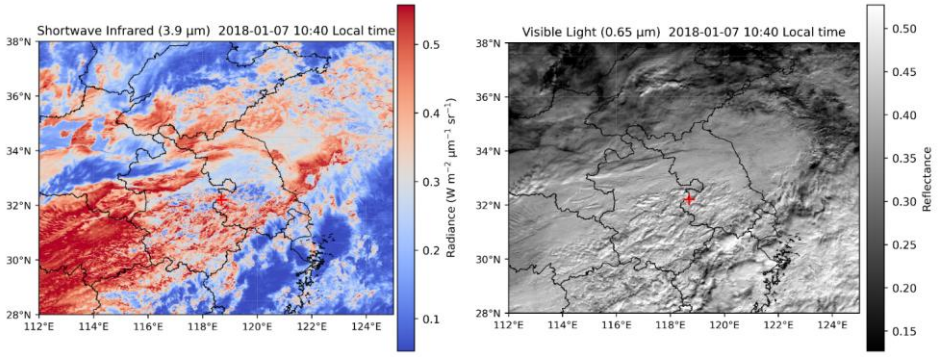

Figure A4 Terra MODIS 3.9 μm shortwave infrared and visible channel imagery for Fog 20, with the observation site marked by a red cross.

带格式的: 正文

A4 A summary table of the 27 fog events, details on the fog types identify and the method used to determine the peak diameters

Table A1 Initial and end times, classification, and mean microphysical properties of the 27 fog events, the first row shows the mean values, in the parentheses are the 25th and 75th percentiles of each characteristic

Fog Case	Initial Time (local time)	End Time (local time)	Type	Modes	Visibility (m)	Wind Spend (m/s)	Temperature (°C)	N_f (cm^{-3})	LWC ($g\ m^{-3}$)	R_v (μm)	R_{eff} (μm)	T	ε	FBS (%)
1-1	2006/12/25 00:10	2006/12/25 13:47	Radiation-advection	triple mode ($3,15,23\mu m$)	240.20 (64.68,123.79)	1.25 (1.07,1.52)	2.95 (1.32,4.36)	352.38 (278.19,440.81)	0.27 (0.16,0.38)	5.37 (1.12,4.72)	8.19 (6.78,9.58)	0.31 (0.06,0.53)	0.78 (0.70,0.87)	37.23 (33.13,39.96)
1-2	2006/12/25 13:48	2006/12/26 14:51	Radiation-advection	triple mode ($3,7,13\mu m$)	375.76 (65.54,264.06)	1.08 (0.62,1.64)	5.24 (4.80,5.63)	349.97 (215.50,524.35)	0.23 (0.07,0.36)	4.79 (3.89,5.65)	7.67 (5.91,9.49)	0.30 (0.04,0.51)	0.75 (0.66,0.88)	42.48 (32.08,49.34)
2	2006/12/26 17:46	2006/12/27 01:36	Radiation-advection	triple mode ($3,9.25\mu m$)	2071.41 (318.75,3909.71)	2.15 (1.94,2.34)	6.22 (6.06,6.36)	136.69 (40.47,224,57)	0.03 (0,0.05)	3.19 (2.53,3.72)	5.10 (3.92,6.01)	0.05 (0,0.06)	0.61 (0.52,0.70)	60.93 (49.47,73.00)
3	2006/12/27 03:28	2006/12/27 12:34	Radiation-advection	single mode ($3\mu m$)	2710.96 (932.30,4119.94)	3.50 (3.33,3.70)	5.26 (5.06,5.34)	70.53 (21.43,108.92)	0.01 (0,0.01)	3.26 (2.69,3.82)	5.78 (4.00,7.54)	0.04 (0,0.05)	0.68 (0.54,0.83)	67.30 (61.06,74.03)
4	2007/12/11 07:06	2007/12/11 09:55	Advection	double mode ($3,13\mu m$)	44.99 (15.00,54.75)	0.40 (0.23,0.58)	2.51 (2.22,2.80)	292.20 (127.70,455.17)	0.11 (0.02,0.20)	4.00 (3.14,4.81)	6.03 (5.41,7.22)	0.01 (0,0.02)	0.72 (0.72,0.82)	58.31 (49.62,67.98)
5	2007/12/14 05:38	2007/12/14 10:20	Radiation	double mode ($3,13\mu m$)	27.39 (15.00,15.00)	0.23 (0,0.39)	-0.09 (-0.88,0.37)	483.12 (396.01,615.34)	0.22 (0.14,0.30)	4.48 (4.00,5.18)	6.85 (6.23,7.84)	0.11 (0.02,0.19)	0.75 (0.72,0.80)	48.59 (43.15,48.46)
6	2007/12/15 04:37	2007/12/15 06:15	Radiation	double mode ($3,9\mu m$)	63.50 (26.50,81.18)	0.02 (0,0)	0.38 (-0.06,0.83)	161.69 (57.69,252.03)	0.01 (0,0.01)	2.18 (2.02,2.29)	2.76 (2.48,2.88)	0	0.42 (0.38,0.44)	73.02 (66.53,81.52)
7	2007/12/15 07:06	2007/12/15 07:37	Radiation	single mode ($3\mu m$)	82.80 (47.25,89.15)	0.04 (0,0)	0 (-0.10,0.12)	140.60 (55.12,170.25)	0.01 (0,0.01)	2.07 (1.95,2.12)	2.60 (2.34,2.69)	0	0.39 (0.36,0.41)	76.75 (73.98,82.12)
8	2007/12/18 06:19	2007/12/18 10:35	Radiation	double mode ($3,12\mu m$)	130.32 (42.69,201.16)	0.28 (0,0.51)	3.99 (3.46,4.30)	205.02 (61.24,316.76)	0.06 (0,0.09)	3.39 (2.25,4.26)	5.55 (2.97,7.17)	0.01 (0,0.02)	0.68 (0.43,0.83)	68.22 (59.18,77.05)
9	2007/12/19 00:23	2007/12/19 11:07	Radiation	double mode ($3,11\mu m$)	78.02 (15.00,117.06)	1.05 (0.20,1.74)	2.34 (0.87,3.60)	261.36 (76.87,355.15)	0.08 (0.01,0.11)	3.65 (3.18,4.25)	5.62 (4.93,6.52)	0.02 (0,0.01)	0.70 (0.66,0.78)	62.99 (52.02,71.12)

10	2007/12/19 22:45	2007/12/20 12:28	Radiation	triple mode (3,11,21μm)	25.75 (15,28.38)	1.38 (0.52,2.14)	3.74 (3.10,4.49)	229.53 (149.03,274.11)	0.06 (0.02,0.07)	3.57 (2.93,3.94)	5.53 (4.35,6.35)	0.04 (0.0,0.02)	0.69 (0.60,0.78)	62.52 (58.21,66.20)
11	2007/12/21 03:39	2007/12/21 08:50	Radiation-advection	triple mode (3,11,23μm)	230.57 (200.00,266.55)	0.91 (0.56,1.20)	7.25 (7.18,7.31)	63.82 (41.87,72.13)	0	2.24 (1.93,2.34)	3.54 (2.54,3.81)	0.01 (0,0)	0.47 (0.37,0.50)	85.60 (84.51,87.73)
12	2007/12/21 12:30	2007/12/21 15:04	Advection	triple mode (3,11,23μm)	131.47 (73.56,166.00)	0.90 (0.50,1.23)	8.20 (8.05,8.37)	165.33 (78.90,242.99)	0.02 (0,0.03)	2.48 (1.92,2.98)	3.90 (2.41,5.09)	0.04 (0,0.05)	0.49 (0.35,0.62)	75.68 (69.42,81.96)
13	2007/12/21 16:30	2007/12/21 17:43	Radiation-advection	double mode (3,9μm)	198.40 (178.50,213.75)	0.47 (0.24,0.69)	8.96 (8.90,9.01)	54.72 (42.92,63.79)	0	2.10 (1.92,2.18)	3.16 (2.50,3.45)	0.01 (0,0)	0.41 (0.35,0.45)	84.50 (83.49,85.11)
14	2007/12/23 01:41	2007/12/23 05:05	Radiation	double mode (3,11μm)	64.93 (26.94,75.13)	0.19 (0,0.31)	5.44 (5.36,5.50)	175.95 (88.42,230.97)	0.05 (0.01,0.06)	3.85 (3.05,4.65)	5.75 (4.42,6.97)	0.01 (0,0.01)	0.71 (0.62,0.80)	58.94 (52.72,64.65)
15	2008/12/04 21:03	2008/12/04 23:39	Radiation	single mode (3μm)	11614.46 (10878.33,12264.17)	3.53 (3.50,3.56)	-0.26 (-0.31,-0.20)	156.01 (84.54,233.95)	0	1.62 (1.45,1.54)	1.96 (1.50,1.69)	0	0.19 (0.10,0.17)	98.71 (98.76,99.51)
16	2009/01/08 08:18	2009/01/08 12:08	Advection	triple mode (3,11,23μm)	120.73 (75.00,150.00)	2.07 (1.98,2.17)	1.76 (1.40,2.12)	146.80 (74.34,199.94)	0.03 (0.01,0.05)	3.99 (3.55,4.50)	6.75 (6.08,7.55)	0.03 (0.01,0.05)	0.79 (0.75,0.84)	62.77 (56.46,65.70)
17	2009/12/01 20:47	2009/12/02 10:42	Radiation	triple mode (3,11,23μm)	108.03 (67.00,91.00)	1.60 (1.07,2.11)	5.14 (3.24,6.33)	233.72 (146.65,323.78)	0.06 (0.02,0.09)	3.67 (3.22,3.99)	6.62 (5.57,7.50)	0.08 (0.02,0.10)	0.78 (0.70,0.87)	68.97 (61.63,72.81)
18	2017/12/31 05:10	2017/12/31 11:00	Radiation	single mode (3μm)	307.77 (60.22,156.26)	0.63 (0.50,0.80)	-0.9 (-1.8,-0.2)	586.26 (368.50,750.63)	0.21 (0.11,0.29)	4.18 (4.60,6.34)	6.34 (6.00,6.93)	0.05 (0.01,0.07)	0.71 (0.68,0.76)	43.71 (37.65,47.48)
19	2018/01/05 21:24	2018/01/05 23:48	Radiation	double mode (3,7μm)	709.46 (178.72,481.12)	0.28 (0,0.50)	-3.04 (-3.80,-2.50)	240.54 (169.28,397.150)	0.06 (0.03,0.10)	3.78 (3.23,4.52)	5.38 (4.51,6.70)	0	0.64 (0.59,0.74)	47.12 (40.71,50.28)
20	2018/01/07 08:41	2018/01/07 12:33	Advection	triple mode (3,9,25μm)	2959.50 (1465.23,3837.43)	1.41 (1.10,1.70)	1.40 (1.30,1.50)	44.52 (19.16,64.95)	0.01 (0.01,0.01)	3.55 (3.08,4.00)	6.45 (5.40,7.37)	0.02 (0,0.03)	0.76 (0.67,0.85)	69.11 (65.63,72.86)
21	2018/11/26 20:47	2018/11/27 08:57	Radiation	triple mode (3,11,23μm)	89.18 (40.00,105.00)	0.56 (0.20,0.90)	9.99 (8.60,11.20)	156.67 (59.92,233.34)	0.13 (0.05,0.17)	6.07 (5.35,6.88)	8.84 (7.97,9.95)	0.23 (0.08,0.35)	0.77 (0.71,0.83)	39.57 (34.03,45.16)
22	2018/11/28 08:00	2018/11/28 09:22	Radiation-advection	single mode (3μm)	296.87 (171.25,422.50)	0.71 (0.40,1.00)	8.23 (7.90,8.50)	98.26 (61.84,133.57)	0.03 (0.02,0.04)	4.41 (4.06,4.71)	7.93 (7.28,8.58)	0.07 (0.04,0.10)	0.87 (0.82,0.92)	67.22 (61.66,71.83)
23	2018/12/01 01:10	2018/12/01 08:08	Radiation-advection	triple mode (3,7,23μm)	373.85 (101.25,600.00)	1.38 (1.00,1.07)	9.77 (9.60,10.00)	108.65 (40.58,170.20)	0.01 (0,0.02)	2.92 (2.50,3.28)	4.77 (3.92,5.26)	0.02 (0,0.01)	0.61 (0.54,0.66)	71.49 (58.97,81.82)
24	2018/12/20 03:22	2018/12/20 08:05	Radiation	double mode (3,7μm)	432.13 (175.00,487.50)	1.17 (0.90,1.40)	9.50 (9.40,9.50)	79.46 (51.24,108.26)	0.01 (0,0.02)	3.12 (2.55,3.67)	4.17 (3.28,5.06)	0	0.54 (0.46,0.62)	52.32 (44.87,59.88)
25	2019/01/04 21:49	2019/01/05 03:50	Radiation	single mode (3μm)	449.48 (295.00,470.00)	1.23 (0.80,1.70)	5.58 (5.20,6.30)	47.38 (30.90,62.06)	0.01 (0,0.01)	2.93 (2.34,3.35)	5.03 (3.39,6.35)	0.05 (0,0.06)	0.59 (0.44,0.71)	72.12 (69.77,75.17)
26	2019/01/06 07:20	2019/01/06 08:39	Rain-induced	triple mode (3,9,25μm)	325.19 (272.50,365.00)	1.65 (1.40,1.90)	2.71 (2.70,2.80)	25.46 (18.44,32.35)	0.01 (0,0.01)	3.99 (3.50,4.45)	7.56 (6.41,8.78)	0.05 (0,0.09)	0.85 (0.75,0.96)	73.39 (69.60,76.49)

Additional details on the fog types identify are provided here. Fog case 6 formed during the night and dissipated around 06:00. According to the observation log, light mist persisted at the site until the formation of Fog case 7, but it did not meet the criteria used in this study to define fog ($N_f > 10$ cm^{-3} and $LWC > 10^{-3}$ g m^{-3}). Therefore, Fog case 6 and Fog case 7 are treated separately, although their formation mechanisms are the same. For Fog case 8, the night preceding fog formation was clear, with strong radiative cooling and very weak winds, conditions favorable for moisture accumulation and fog development. Fog case 8 is therefore classified as a radiation fog. Fog case 26 developed in the morning. Light drizzle occurred the previous afternoon, followed by light mist during the night, indicating that precipitation played a role in its formation.

The peak mode number and peak diameters for each fog event in this table were determined as follows. The peak number was assigned based on the most frequently occurring DSD type (unimodal, bimodal or trimodal) within the event. Once the peak number was identified, the peak diameters were defined as the median diameters of the bins with the highest occurrence

frequencies. For a trimodal event, for example, the three bins with the highest frequencies were used to determine the three peak diameters.

Table A1 Initial and end times, classification, and mean microphysical properties of the 27 fog events

Fog Case	Initial Time (UTC+8)	End Time (UTC+8)	Type	N_F (cm^{-3})	LWC ($g\ m^{-3}$)	R_v (μm)	R_{eff} (μm)	T	ε	FBS (%)
1-1	2006/12/25 00:10	2006/12/25 13:47	triple mode ($3,15,21\mu m$)	351.56	0.27	5.37	8.18	0.31	0.78	37.23
1-2	2006/12/25 13:48	2006/12/26 14:51	double mode ($3,21\mu m$)	349.97	0.23	4.79	7.67	0.30	0.75	42.48
2	2006/12/26 17:46	2006/12/27 01:36	double mode ($3,21\mu m$)	134.19	0.03	3.17	5.07	0.05	0.61	61.21
3	2006/12/27 03:28	2006/12/27 12:34	double mode ($3,21\mu m$)	68.47	0.01	3.32	5.98	0.04	0.69	67.33
4	2007/12/11 07:06	2007/12/11 09:55	triple mode ($3,13,21\mu m$)	302.68	0.11	4.00	6.02	0.01	0.72	58.31
5	2007/12/14 05:38	2007/12/14 10:20	triple mode ($3,13,21\mu m$)	489.08	0.22	4.51	6.87	0.12	0.75	47.73
6	2007/12/15 04:37	2007/12/15 06:15	single mode ($3\mu m$)	167.97	0.01	2.14	2.65	0	0.41	69.91
7	2007/12/15 07:06	2007/12/15 07:37	single mode ($3\mu m$)	152.81	0.01	2.05	2.53	0	0.39	73.63
8	2007/12/18 06:19	2007/12/18 10:35	triple mode ($3,13,21\mu m$)	199.37	0.05	3.32	5.39	0.01	0.66	68.44
9	2007/12/19 00:23	2007/12/19 11:07	triple mode ($3,13,21\mu m$)	254.74	0.08	3.58	5.47	0.02	0.69	63.22
10	2007/12/19 22:45	2007/12/20 12:28	triple mode ($3,13,21\mu m$)	231.02	0.06	3.58	5.54	0.04	0.69	62.17
11	2007/12/21 03:39	2007/12/21 08:50	double mode ($3,21\mu m$)	64.50	0	2.23	3.52	0.01	0.46	85.50
12	2007/12/21 12:30	2007/12/21 15:04	double mode ($3,21\mu m$)	168.93	0.02	2.51	3.97	0.04	0.50	75.33
13	2007/12/21 16:30	2007/12/21 17:43	single mode ($3\mu m$)	56.97	0	2.08	3.13	0.01	0.40	84.45
14	2007/12/23 01:41	2007/12/23 05:05	triple mode ($3,13,21\mu m$)	179.63	0.05	3.87	5.75	0.01	0.71	58.19
15	2008/12/04 21:03	2008/12/04 23:39	single mode ($3\mu m$)	154.97	0	1.62	1.96	0	0.19	98.79
16	2009/01/08 08:18	2009/01/08 12:08	double mode ($3,21\mu m$)	146.75	0.03	3.95	6.64	0.03	0.78	61.47
17	2009/12/01 20:47	2009/12/02 10:42	double mode ($3,21\mu m$)	234.55	0.06	3.67	6.59	0.09	0.77	68.74
18	2017/12/31 05:10	2017/12/31 11:00	double mode ($3,21\mu m$)	597.88	0.21	4.19	6.33	0.05	0.72	43.00
19	2018/01/05 21:24	2018/01/05 23:48	triple mode ($3,13,21\mu m$)	249.77	0.06	3.77	5.34	0	0.63	46.08
20	2018/01/07 08:41	2018/01/07 12:33	double mode ($3,21\mu m$)	44.20	0.01	3.55	6.38	0.02	0.75	69.38
21	2018/11/26 20:47	2018/11/27 08:57	triple mode ($3,11,21\mu m$)	164.68	0.13	6.02	8.80	0.22	0.77	40.53

22	2018/11/28 08:00	2018/11/28 09:22	double mode (3,21μm)	104.31	0.03	4.41	7.87	0.07	0.86	66.18
23	2018/12/01 01:10	2018/12/01 08:08	double mode (3,21μm)	107.65	0.01	2.88	4.71	0.02	0.61	71.75
24	2018/12/20 03:22	2018/12/20 08:05	double mode (3,21μm)	80.27	0.01	3.09	4.12	0	0.53	52.50
25	2019/01/04 21:49	2019/01/05 03:50	double mode (3,21μm)	48.77	0.01	2.83	4.75	0.04	0.56	72.61
26	2019/01/06 07:20	2019/01/06 08:39	double mode (3,21μm)	25.70	0.01	4.06	7.75	0.06	0.87	73.22

A5 Additional figures to be included

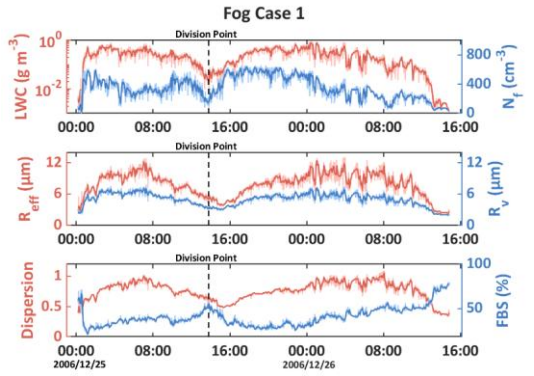

Figure A5 the temporal evolution of N_f, LWC, R_v, R_{eff}, FBS and dispersion for fog case 1, the dark lines represent 5-minute averaged values while the light lines are 1-minute averaged values, the black dashed line is the boundary between F1-1 and F1-2

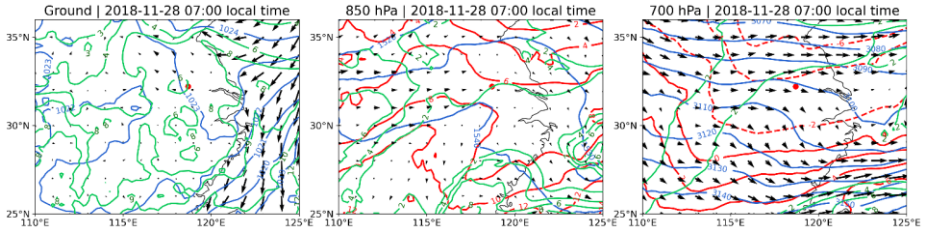

Figure A6 Synoptic conditions of Fog 22. Red dots indicate observation stations; blue lines represent isobars or geopotential height contours; red lines are isotherms, dashed when temperatures are below 0 °C; green lines denote constant specific humidity.

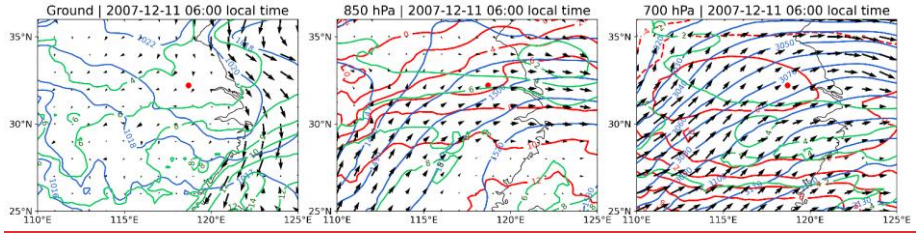

Figure A7 Synoptic conditions of Fog 4.

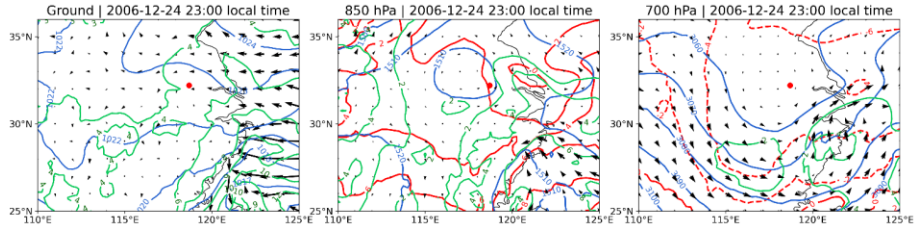

Figure A8 Synoptic conditions of Fog 1-1.

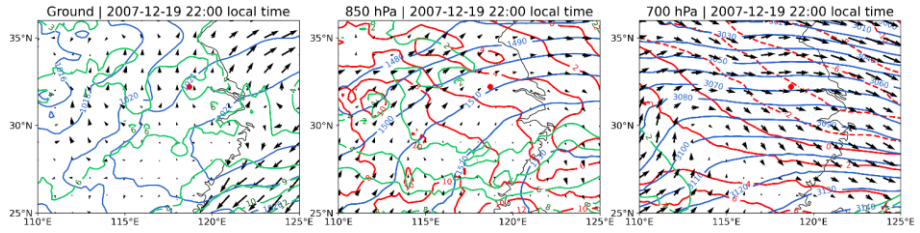

Figure A9 Synoptic conditions of Fog 10.

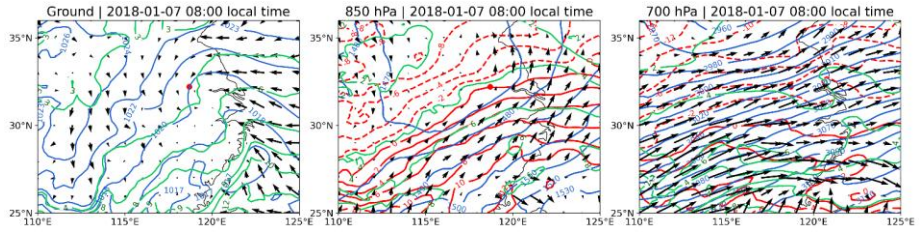

Figure A10 Synoptic conditions of Fog 20.

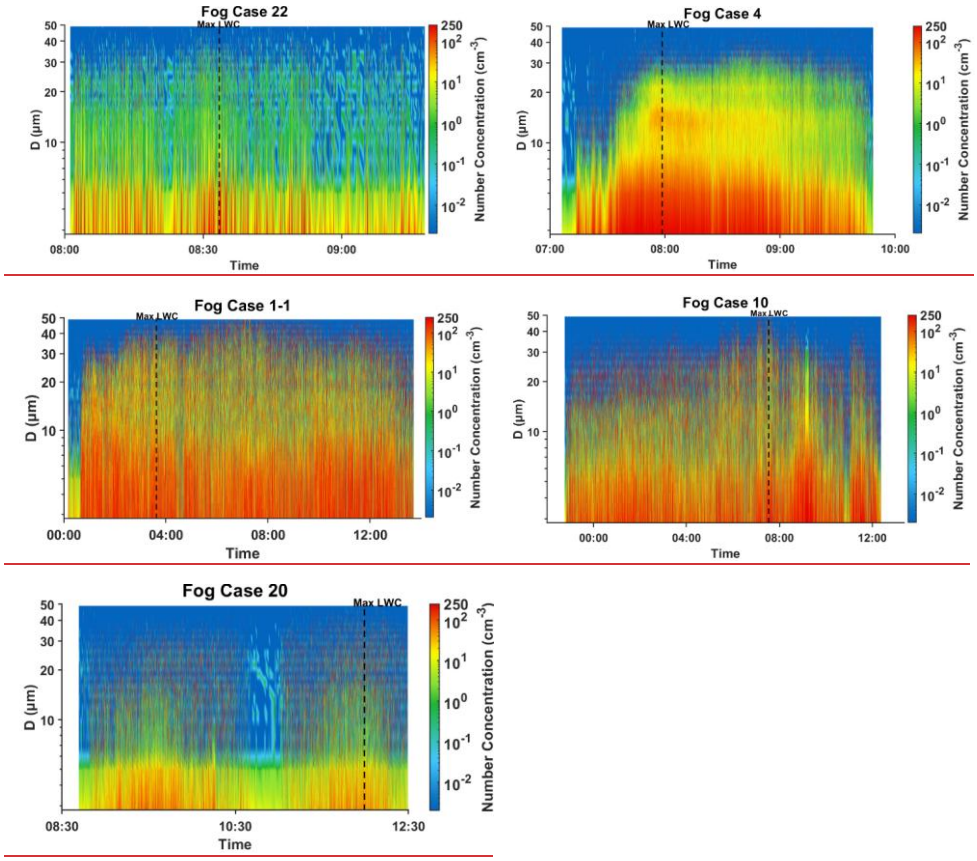

Figure A11 The time series of DSDs at 1s resolution of Fog Case 22, Fog Case 4, Fog Case 1-1, Fog Case 10 and Fog Case 20

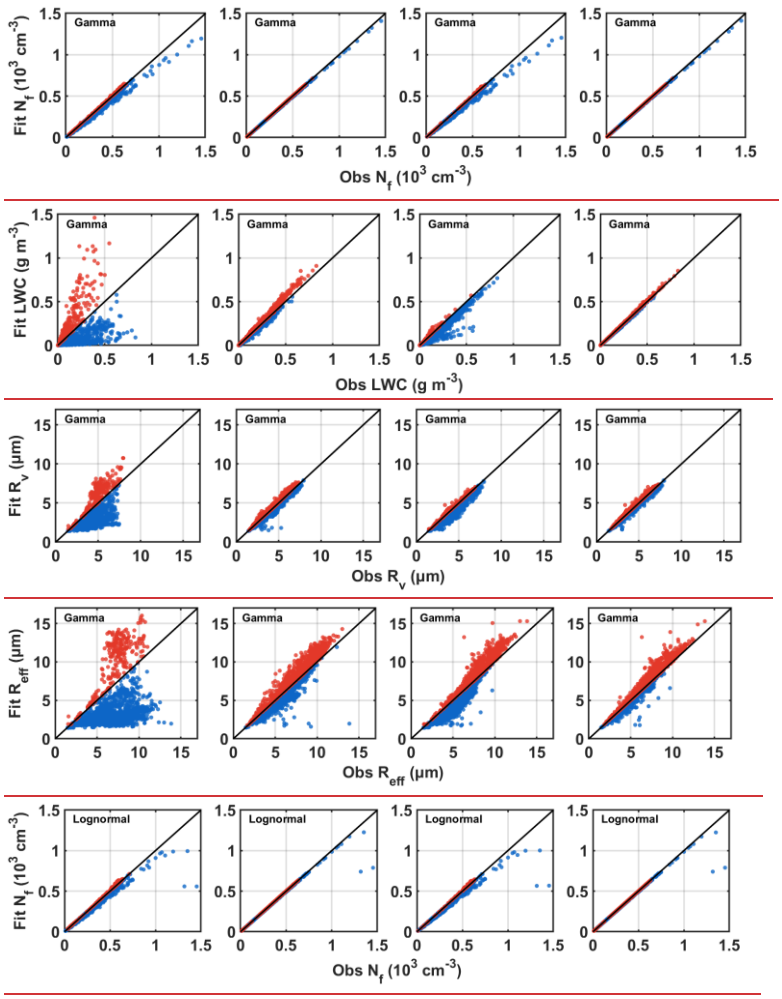
Gamma
Fit N_f (10^3 cm^{-3})
Obs N_f (10^3 cm^{-3})
Gamma
Fit LWC (g m^{-3})
Obs LWC (g m^{-3})
Gamma
Fit R_v (μm)
Obs R_v (μm)
Gamma
Fit R_{eff} (μm)
Obs R_{eff} (μm)
Lognormal
Fit N_f (10^3 cm^{-3})
Obs N_f (10^3 cm^{-3})

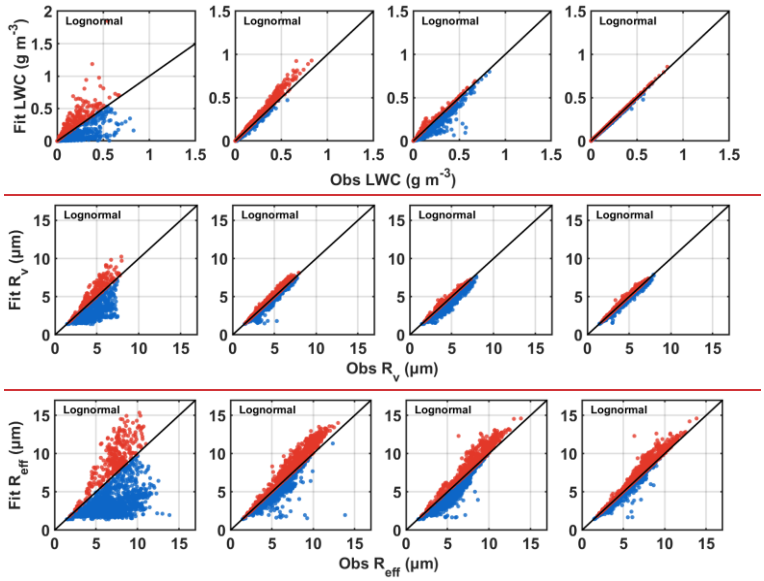

Figure A12 Correlation between N_f, LWC, R_v and R_{eff} derived from observed spectrum and those computed from the gamma and lognormal fitted spectrum with no breakpoint (first column), breakpoint at 10 μm (second column), breakpoint at 22 μm (third column) and breakpoint at 10 μm and 22 μm (fourth column). Red dots indicate overestimation of the microphysical properties by the gamma fit, while blue dots indicate underestimation.

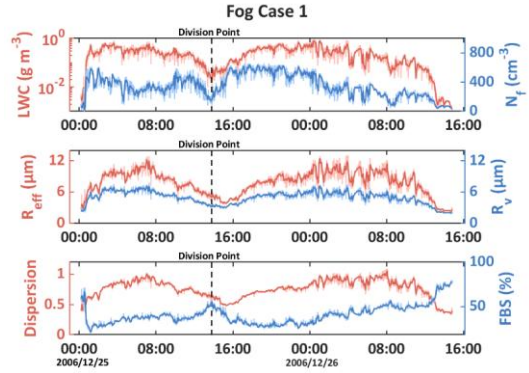

~~Figure A1 the temporal evolution of N_d, LWC, R_v, R_{eff}, FBS and dispersion for fog case 1, the dark lines represent 5-minute averaged values while the light lines are 1-minute averaged values, the black dashed line is the boundary between F1-1 and F1-2~~

Data availability

Fog DSD data used in this study is available at Zenodo: https://doi.org/10.5281/zenodo.16883670 . Except for fog case 1-3 and 18-20, where visibility was calculated using Eq.(9) and (10), visibility data for other cases were obtained from PWD measurements. Meteorological variables including temperature, wind speed, and wind direction were sourced from the Nanjing University of Information Science and Technology (NUIST) automatic weather station, except for wind speed in fog case 1-3 and temperature, wind speed, and wind direction in fog case 15-17, which were taken from https://cds.climate.copernicus.eu/datasets/reanalysis-era5-single-levels?tab=overview (ERA5 hourly data on single levels from 1940 to present). Synoptic conditions for all fog cases were derived from https://cds.climate.copernicus.eu/datasets (ERA5 hourly data on pressure levels from 1940 to present and ERA5 hourly data on single levels from 1940 to present). The satellite imagery in the appendix (Figures A2-A4) is obtained from Home - LAADS DAAC (Aqua MODIS and Terra MODIS). ~~Data used in this study is available at Zenodo: https://doi.org/10.5281/zenodo.16883670 .~~

Author contributions

JZ and XL shaped the concept of this study and performed data analysis. JZ prepared the figures and wrote the initial draft. XL supervised this work and revised the article. ZA gave suggestions on data processing and visualization. JL provided guidance for the synoptic analysis. DX provided guidance on locating and downloading the MODIS data.

Acknowledgements

We gratefully acknowledge Professor Shengjie Niu and his research team for their efforts in acquiring and sharing the fog microphysical observation data that supported this study. We would like to acknowledge the High Performance Computing Center of Nanjing University of Information Science and Technology and the National Key Scientific and Technological Infrastructure project “Earth System Numerical Simulation Facility” (EarthLab) for their support of this work.

Financial support

This study was supported by the National Natural Science Foundation of China (GrantNos.42061134009 and 41975176) and the National Key Scientific and Technological Infrastructure project “Earth System Numerical Simulation Facility” (EarthLab).

Reference

Boudala, F. S., Wu, D., Isaac, G. A., and Gultepe, I.: Seasonal and Microphysical Characteristics of Fog at a Northern Airport in Alberta, Canada, Remote Sensing, 14, 4865, https://doi.org/10.3390/rs14194865, 2022.

Boutle, I., Price, J., Kudzotsa, I., Kokkola, H., and Romakkaniemi, S.: Aerosol–fog interaction and the transition to well-mixed radiation fog, Atmos Chem Phys, 18, 7827–7840, https://doi.org/10.5194/acp-18-7827-2018, 2018.

Boutle, I., Angevine, W., Bao, J.-W., Bergot, T., Bhattacharya, R., Bott, A., Ducongé, L., Forbes, R., Goecke, T., Grell, E., Hill, A., Igel, A. L., Kudzotsa, I., Lac, C., Maronga, B., Romakkaniemi, S., Schmidli, J., Schwenkel, J., Steeneveld, G.-J., and Vié, B.: Demistify: a large-eddy simulation (LES) and single-column model (SCM) intercomparison of radiation fog, Atmos Chem Phys, 22, 319–333, https://doi.org/10.5194/acp-22-319-2022, 2022.

Brenguier, J.-L., Pawlowska, H., Schüller, L., Preusker, R., Fischer, J., and Fouquart, Y.: Radiative Properties of Boundary Layer Clouds: Droplet Effective Radius versus Number Concentration, J. Atmospheric Sci., 57, 803–821, https://doi.org/10.1175/1520-0469(2000)057%253C0803:RPOBLC%253E2.0.CO;2, 2000.

Brown, R.: A numerical study of radiation fog with an explicit formulation of the microphysics, Quarterly Journal of the Royal Meteorological Society, 106, 781–802, https://doi.org/10.1002/qj.49710645010, 1980.

Chakrabarti, A. and Ghosh, J. K.: AIC, BIC and Recent Advances in Model Selection, in: Philosophy of Statistics, vol. 7, edited by: Bandyopadhyay, P. S. and Forster, M. R., North-Holland, Amsterdam, 583–605, https://doi.org/10.1016/B978-0-444-51862-0.50018-6, 2011.

Chen, J., Liu, Y., Zhang, M., and Peng, Y.: New understanding and quantification of the regime dependence of aerosol-cloud interaction for studying aerosol indirect effects, Geophys. Res. Lett., 43, 1780–1787, https://doi.org/10.1002/2016GL067683, 2016.

Cui, C., Bao, Y., Yuan, C., Li, Z., and Zong, C.: Comparison of the performances between the WRF and WRF-LES models in radiation fog – A case study, Atmospheric Res., 226, 76–86, https://doi.org/10.1016/j.atmosres.2019.04.003, 2019.

Dorman, C. E., Hoch, S. W., Gultepe, I., Wang, Q., Yamaguchi, R. T., Fernando, H. J. S., and Krishnamurthy, R.: Large-Scale Synoptic Systems and Fog During the C-FOG Field Experiment, Boundary-Layer Meteorology, 181, 171–202, https://doi.org/10.1007/s10546-021-00641-1, 2021.

Elias, T., Dupont, J.-C., Hammer, E., Hoyle, C. R., Haeffelin, M., Burnet, F., and Jolivet, D.: Enhanced extinction of visible radiation due to hydrated aerosols in mist and fog, Atmospheric Chemistry and Physics, 15, 6605–6623, https://doi.org/10.5194/acp-15-6605-2015, 2015.

Elias, T., Haeffelin, M., Drobinski, P., Gomes, L., Rangognio, J., Bergot, T., Chazette, P., Raut, J.-C., and Colomb, M.: Particulate contribution to extinction of visible radiation: Pollution, haze, and fog, Atmospheric Res., 92, 443–454, https://doi.org/10.1016/j.atmosres.2009.01.006, 2009.

Friedlein, M. T.: DENSE FOG CLIMATOLOGY, Bulletin of the American Meteorological Society, 85, 515–517, 2004.

设置了格式: 英语(美国)

设置了格式: 字体: (中文) +中文正文 (等线), (中文) 简体中文(中国大陆), (其他) 英语(美国)

设置了格式: 字体: (中文) +中文正文 (等线), (中文) 简体中文(中国大陆), (其他) 英语(美国)

设置了格式: 字体: (中文) +中文正文 (等线), (中文) 简体中文(中国大陆), (其他) 英语(美国)

Ge, P., Zhang, Y., Fan, S., Wang, Y., Wu, H., Wang, X., and Zhang, S.: Observational study of microphysical and chemical characteristics of size-resolved fog in different regional backgrounds in China, Sci. Total Environ., 950, 175329, https://doi.org/10.1016/j.scitotenv.2024.175329, 2024.

Gultepe, I., Heymsfield, A. J., Fernando, H. J. S., Pardyjak, E., Dorman, C. E., Wang, Q., Creegan, E., Hoch, S. W., Flagg, D. D., Yamaguchi, R., Krishnamurthy, R., Gaberšek, S., Perrie, W., Perelet, A., Singh, D. K., Chang, R., Nagare, B., Wagh, S., and Wang, S.: A Review of Coastal Fog Microphysics During C-FOG, Boundary-Layer Meteorology, 181, 227–265, https://doi.org/10.1007/s10546-021-00659-5, 2021.

Gultepe, I., Kuhn, T., Pavolonis, M., Calvert, C., Gurka, J., Heymsfield, A. J., Liu, P. S. K., Zhou, B., Ware, R., Ferrier, B., Milbrandt, J., and Bernstein, B.: Ice Fog in Arctic During FRAM–Ice Fog Project: Aviation and Nowcasting Applications, Bull. Am. Meteorol. Soc., 95, 211–226, https://doi.org/10.1175/BAMS-D-11-00071.1, 2014.

Gultepe, I. and Milbrandt, J. A.: Microphysical Observations and Mesoscale Model Simulation of a Warm Fog Case during FRAM Project, in: Fog and Boundary Layer Clouds: Fog Visibility and Forecasting, Basel, 1161–1178, 2007.

Gultepe, I. and Milbrandt, J. A.: Probabilistic Parameterizations of Visibility Using Observations of Rain Precipitation Rate, Relative Humidity, and Visibility, J. Appl. Meteorol. Climatol., 49, 36–46, https://doi.org/10.1175/2009JAMC1927.1, 2010.

Gultepe, I., Müller, M. D., and Boybeyi, Z.: A New Visibility Parameterization for Warm-Fog Applications in Numerical Weather Prediction Models, J. Appl. Meteorol. Climatol., 45, 1469–1480, https://doi.org/10.1175/JAM2423.1, 2006.

Gultepe, I., Tardif, R., Michaelides, S. C., Cermak, J., Bott, A., Bendix, J., Müller, M. D., Pagowski, M., Hansen, B., Ellrod, G., Jacobs, W., Toth, G., and Cober, S. G.: Fog Research: A Review of Past Achievements and Future Perspectives, Pure Appl. Geophys., 164, 1121–1159, https://doi.org/10.1007/s00024-007-0211-x, 2007.

Gultepe, I., Pearson, G., Milbrandt, J. A., Hansen, B., Platnick, S., Taylor, P., Gordon, M., Oakley, J. P., and Cober, S. G.: The Fog Remote Sensing and Modeling Field Project, Bull. Am. Meteorol. Soc., 90, 341–360, https://doi.org/10.1175/2008BAMS2354.1, 2009.

Guo, L., Guo, X., Fang, C., and Zhu, S.: Observation analysis on characteristics of formation, evolution and transition of a long-lasting severe fog and haze episode in North China, Sci. China Earth Sci., 58, 329–344, https://doi.org/10.1007/s11430-014-4924-2, 2015.

Haeffelin, M., Bergot, T., Elias, T., Tardif, R., Carrer, D., Chazette, P., Colomb, M., Drobinski, P., Dupont, E., Dupont, J.-C., Gomes, L., Musson-Genon, L., Pietras, C., Plana-Fattori, A., Protat, A., Rangognio, J., Raut, J.-C., Rémy, S., Richard, D., Sciare, J., and Zhang, X.: Parisfog: Shedding new Light on Fog Physical Processes, Bull. Am. Meteorol. Soc., 91, 767–783, https://doi.org/10.1175/2009BAMS2671.1, 2010.

Hammer, E., Gysel, M., Roberts, G. C., Elias, T., Hofer, J., Hoyle, C. R., Bukowiecki, N., Dupont, J.-C., Burnet, F., Baltensperger, U., and Weingartner, E.: Size-dependent particle activation properties in fog during the ParisFog 2012/13 field campaign, Atmospheric Chemistry and Physics, 14, 10517–10533, https://doi.org/10.5194/acp-14-10517-2014, 2014.

H. Akaike: A new look at the statistical model identification, IEEE Trans. Autom. Control, 19, 716–723, https://doi.org/10.1109/TAC.1974.1100705, 1974.

设置了格式: 字体: (中文) +中文正文 (等线), (中文) 简体中文(中国大陆), (其他) 英语(美国)

设置了格式: 字体: (中文) +中文正文 (等线), (中文) 简体中文(中国大陆), (其他) 英语(美国)

设置了格式: 字体: (中文) +中文正文 (等线), (中文) 简体中文(中国大陆)

Jia, X., Quan, J., Zheng, Z., Liu, X., Liu, Q., He, H., and Liu, Y.: Impacts of Anthropogenic Aerosols on Fog in North China Plain, J. Geophys. Res. Atmospheres, 124, 252–265, https://doi.org/10.1029/2018JD029437, 2019.

Kessler, E.: On the Distribution and Continuity of Water Substance in Atmospheric Circulations, in: On the Distribution and Continuity of Water Substance in Atmospheric Circulations, edited by: Kessler, E., American Meteorological Society, Boston, MA, 1–84, https://doi.org/10.1007/978-1-935704-36-2_1, 1969.

KOENIG, L. R.: NUMERICAL EXPERIMENTS PERTAINING TO WARM-FOG CLEARING, Mon. Weather Rev., 99, 227–241, https://doi.org/10.1175/1520-0493(1971)099%253C0227:NEPTWC%253E2.3.CO;2, 1971.

Koračin, D., Dorman, C. E., Lewis, J. M., Hudson, J. G., Wilcox, E. M., and Torregrosa, A.: Marine fog: A review, Atmospheric Research, 143, 142–175, https://doi.org/10.1016/j.atmosres.2013.12.012, 2014.

Khain, A. P., Beheng, K. D., Heymsfield, A., Korolev, A., Krichak, S. O., Levin, Z., Pinsky, M., Phillips, V., Prabhakaran, T., Teller, A., van den Heever, S. C., and Yano, J.-I.: Representation of microphysical processes in cloud-resolving models: Spectral (bin) microphysics versus bulk parameterization, Rev. Geophys., 53, 247–322, https://doi.org/10.1002/2014RG000468, 2015.

Kunkel, B. A.: Microphysical properties of fog at Otis AFB, Air Force Geophysics Laboratories, Air Force Systems Command, United States …, 1982.

Lakra, K. and Avishek, K.: A review on factors influencing fog formation, classification, forecasting, detection and impacts, Rendiconti Lincei Sci. Fis. E Nat., 33, 319–353, https://doi.org/10.1007/s12210-022-01060-1, 2022.

Li, J., Wang, X., Chen, J., Zhu, C., Li, W., Li, C., Liu, L., Xu, C., Wen, L., Xue, L., Wang, W., Ding, A., and Herrmann, H.: Chemical composition and droplet size distribution of cloud at the summit of Mount Tai, China, Atmos Chem Phys, 17, 9885–9896, https://doi.org/10.5194/acp-17-9885-2017, 2017.

Liu, D., Yang, J., Niu, S., and Li, Z.: On the evolution and structure of a radiation fog event in Nanjing, Adv. Atmospheric Sci., 28, 223–237, https://doi.org/10.1007/s00376-010-0017-0, 2011.

Liu, Y. and Daum, P. H.: Indirect warming effect from dispersion forcing, Nature, 419, 580–581, https://doi.org/10.1038/419580a, 2002.

Lu, C., Liu, Y., Niu, S., Zhao, L., Yu, H., and Cheng, M.: Examination of microphysical relationships and corresponding microphysical processes in warm fogs, Acta Meteorol. Sin., 27, 832–848, https://doi.org/10.1007/s13351-013-0610-0, 2013.

Lu, C., Liu, Y., Yum, S. S., Chen, J., Zhu, L., Gao, S., Yin, Y., Jia, X., and Wang, Y.: Reconciling Contrasting Relationships Between Relative Dispersion and Volume-Mean Radius of Cloud Droplet Size Distributions, J. Geophys. Res. Atmospheres, 125, e2019JD031868, https://doi.org/10.1029/2019JD031868, 2020.

Martinet, P., Cimini, D., Burnet, F., Ménétrier, B., Michel, Y., and Unger, V.: Improvement of numerical weather prediction model analysis during fog conditions through the assimilation of ground-based microwave radiometer observations: a 1D-Var study, Atmos Meas Tech, 13, 6593–6611, https://doi.org/10.5194/amt-13-6593-2020, 2020.

设置了格式: 字体: (中文) +中文正文 (等线), (中文) 简体中文(中国大陆), (其他) 英语(美国)

设置了格式: 字体: (中文) +中文正文 (等线), (中文) 简体中文(中国大陆), (其他) 英语(美国)

Mazoyer, M., Lac, C., Thouron, O., Bergot, T., Masson, V., and Musson-Genon, L.: Large eddy simulation of radiation fog: impact of dynamics on the fog life cycle, Atmos Chem Phys, 17, 13017–13035, https://doi.org/10.5194/acp-17-13017-2017, 2017.

Mazoyer, M., Burnet, F., and Denjean, C.: Experimental study on the evolution of droplet size distribution during the fog life cycle, Atmos Chem Phys, 22, 11305–11321, https://doi.org/10.5194/acp-22-11305-2022, 2022.

Meyer, M. B., Jiusto, J. E., and Lala, G. G.: Measurements of visual range and radiation-fog (haze) microphysics, Journal of Atmospheric Sciences, 37, 622–629, 1980.

Nelli, N., Francis, D., Abida, R., Fonseca, R., Masson, O., and Bosc, E.: In-situ measurements of fog microphysics: Visibility parameterization and estimation of fog droplet sedimentation velocity, Atmospheric Res., 309, 107570, https://doi.org/10.1016/j.atmosres.2024.107570, 2024.

Niu, S., Lu, C., Liu, Y., Zhao, L., Lü, J., and Yang, J.: Analysis of the microphysical structure of heavy fog using a droplet spectrometer: A case study, Adv. Atmospheric Sci., 27, 1259–1275, https://doi.org/10.1007/s00376-010-8192-6, 2010.

Niu, S. J., Liu, D. Y., Zhao, L. J., Lu, C. S., Lü, J. J., and Yang, J.: Summary of a 4-Year Fog Field Study in Northern Nanjing, Part 2: Fog Microphysics, Pure Appl. Geophys., 169, 1137–1155, https://doi.org/10.1007/s00024-011-0344-9, 2012.

Payra, S. and Mohan, M.: Multirule Based Diagnostic Approach for the Fog Predictions Using WRF Modelling Tool, Adv. Meteorol., 2014, 456065, https://doi.org/10.1155/2014/456065, 2014.

Peterka, A., Thompson, G., and Geresdi, I.: Numerical prediction of fog: A novel parameterization for droplet formation, Q. J. R. Meteorol. Soc., 150, 2203–2222, https://doi.org/10.1002/qj.4704, 2024.

Pinnick, R. G., Hoihjelle, D. L., Fernandez, G., Stenmark, E. B., Lindberg, J. D., Hoidale, G. B., and Jennings, S. G.: Vertical Structure in Atmospheric Fog and Haze and Its Effects on Visible and Infrared Extinction, Journal of Atmospheric Sciences, 35, 2020–2032, https://doi.org/10.1175/1520-0469(1978)035%253C2020:VSIAFA%253E2.0.CO;2, 1978.

Price, J. D.: On the Formation and Development of Radiation Fog: An Observational Study, Bound.-Layer Meteorol., 172, 167–197, https://doi.org/10.1007/s10546-019-00444-5, 2019.

Roach, W. T.: On the effect of radiative exchange on the growth by condensation of a cloud or fog droplet, Quarterly Journal of the Royal Meteorological Society, 102, 361–372, https://doi.org/10.1002/qj.49710243207, 1976.

Roach, W. T., Brown, R., Caughey, S. J., Garland, J. A., and Readings, C. J.: The physics of radiation fog: I – a field study, Quarterly Journal of the Royal Meteorological Society, 102, 313–333, https://doi.org/10.1002/qj.49710243204, 1976.

Román-Cascón, C., Steeneveld, G. J., Yagüe, C., Sastre, M., Arrillaga, J. A., and Maqueda, G.: Forecasting radiation fog at climatologically contrasting sites: evaluation of statistical methods and WRF, Q. J. R. Meteorol. Soc., 142, 1048–1063, https://doi.org/10.1002/qj.2708, 2016.

Ryznar, E.: Advection-radiation fog near lake Michigan, Atmospheric Environment (1967), 11, 427–430, https://doi.org/10.1016/0004-6981(77)90004-X, 1977.

Sampurno Bruijnzeel, L., Eugster, W., and Burkard, R.: Fog as a Hydrologic Input, in: Encyclopedia of Hydrological Sciences, https://doi.org/10.1002/0470848944.hsa041, 2005.

设置了格式: 字体: (中文) +中文正文 (等线), (中文) 简体中文(中国大陆), (其他) 英语(美国)

设置了格式: 字体: (中文) +中文正文 (等线), (中文) 简体中文(中国大陆), (其他) 英语(美国)

设置了格式: 字体: (中文) +中文正文 (等线), (中文) 简体中文(中国大陆), (其他) 英语(美国)

Schwarz, G.: Estimating the Dimension of a Model, Ann. Stat., 6, 461–464, 1978.

Shao, N., Lu, C., Jia, X., Wang, Y., Li, Y., Yin, Y., Zhu, B., Zhao, T., Liu, D., Niu, S., Fan, S., Yan, S., and Lv, J.: Radiation fog properties in two consecutive events under polluted and clean conditions in the Yangtze River Delta, China: a simulation study, Atmos Chem Phys, 23, 9873–9890, https://doi.org/10.5194/acp-23-9873-2023, 2023.

Shen, C., Zhao, C., Ma, N., Tao, J., Zhao, G., Yu, Y., and Kuang, Y.: Method to Estimate Water Vapor Supersaturation in the Ambient Activation Process Using Aerosol and Droplet Measurement Data, J. Geophys. Res. Atmospheres, 123, 10,606-10,619, https://doi.org/10.1029/2018JD028315, 2018.

Stephens, G. L.: Radiation Profiles in Extended Water Clouds. I: Theory, J. Atmospheric Sci., 35, 2111–2122, https://doi.org/10.1175/1520-0469(1978)035<2111:RPIEWC>2.0.CO;2, 1978.

Stephens, G. L.: The Parameterization of Radiation for Numerical Weather Prediction and Climate Models, Mon. Weather Rev., 112, 826–867, https://doi.org/10.1175/1520-0493(1984)112<0826:TPORFN>2.0.CO;2, 1984.

Stewart, D. A. and Essenwanger, O. M.: A survey of fog and related optical propagation characteristics, Reviews of Geophysics, 20, 481–495, https://doi.org/10.1029/RG020i003p00481, 1982.

Symonds, M. R. E. and Moussalli, A.: A brief guide to model selection, multimodel inference and model averaging in behavioural ecology using Akaike's information criterion, Behavioral Ecology and Sociobiology, 65, 13–21, https://doi.org/10.1007/s00265-010-1037-6, 2011.

Tampieri, F. and Tomasi, C.: Size distribution models of fog and cloud droplets in terms of the modified gamma function, Tellus, 28, 333–347, https://doi.org/10.3402/tellusa.v28i4.10300, 1976.

Tudor, M.: Impact of horizontal diffusion, radiation and cloudiness parameterization schemes on fog forecasting in valleys, Meteorol. Atmospheric Phys., 108, 57–70, https://doi.org/10.1007/s00703-010-0084-x, 2010.

Turton, J. D. and Brown, R.: A comparison of a numerical model of radiation fog with detailed observations, Quarterly Journal of the Royal Meteorological Society, 113, 37–54, https://doi.org/10.1002/qj.49711347504, 1987.

Twomey, S. and Bohren, C. F.: Simple Approximations for Calculations of Absorption in Clouds, J. Atmospheric Sci., 37, 2086–2095, https://doi.org/10.1175/1520-0469(1980)037<2086:SAFCOA>2.0.CO;2, 1980.

Wang, H., Zhang, Z., Liu, D., Zhu, Y., Zhang, X., and Yuan, C.: Study on a Large-Scale Persistent Strong Dense Fog Event in Central and Eastern China, Adv. Meteorol., 2020, 8872334, https://doi.org/10.1155/2020/8872334, 2020.

~~Wang, Q., Fan, M., Li, J., and Zhang, H.: The microphysical characteristics of winter fog in Jinan and its effect on visibility (in Chinese), Chinese Journal of Atmospheric Sciences, 45, 333–354, https://doi.org/10.3878/j.issn.1006-9895.2011.19248, 2021a.~~

Wang, Y., Niu, S., Lv, J., Lu, C., Xu, X., Wang, Y., Ding, J., Zhang, H., Wang, T., and Kang, B.: A New Method for Distinguishing Unactivated Particles in Cloud Condensation Nuclei Measurements: Implications for Aerosol Indirect Effect Evaluation, Geophys. Res. Lett., 46, 14185–14194, https://doi.org/10.1029/2019GL085379, 2019.

设置了格式: 字体: (中文) +中文正文 (等线), (中文) 简体中文(中国大陆)

设置了格式: 字体: (中文) +中文正文 (等线), (中文) 简体中文(中国大陆), (其他) 英语(美国)

设置了格式: 字体: (中文) +中文正文 (等线), (中文) 简体中文(中国大陆), (其他) 英语(美国)

Wang, Y., Niu, S., Lu, C., Lv, J., Zhang, J., Zhang, H., Zhang, S., Shao, N., Sun, W., Jin, Y., and Song, Q.: Observational study of the physical and chemical characteristics of the winter radiation fog in the tropical rainforest in Xishuangbanna, China, Sci. China Earth Sci., 64, 1982–1995, https://doi.org/10.1007/s11430-020-9766-4, 2021b.

Wendisch, M., Mertes, S., Heintzenberg, J., Wiedensohler, A., Schell, D., Wobrock, W., Frank, G., Martinsson, B. G., Fuzzi, S., and Orsi, G.: Drop size distribution and LWC in Po Valley fog, Contributions to atmospheric physics, 71, 1998.

WILLETT, H. C.: FOG AND HAZE, THEIR CAUSES, DISTRIBUTION, AND FORECASTING, Monthly Weather Review, 56, 435–468, https://doi.org/10.1175/1520-0493(1928)56%253C435:FAHTCD%253E2.0.CO;2, 1928.

Zhang, J., Yang, Y., and Ding, J.: Information criteria for model selection, WIREs Comput. Stat., 15, e1607, https://doi.org/10.1002/wics.1607, 2023.

设置了格式: 字体: (中文) + 中文正文 (等线), (中文) 简体中文(中国大陆)